Projecte Final del Grau en
Enginyeria Física

Hole-selective contacts by RF magnetron sputtering for silicon heterojunction solar cell structures

Raül Perea Causín

Directors:
Cristóbal Voz Sánchez
Joan Bertomeu Balagueró

Universitat Politècnica de Catalunya

Barcelona,
Juny 2017

A la Gemma,
als meus pares i
al meu germà

Abstract

Research in photovoltaic devices is focusing towards cost-effective technologies to compete with traditional energy sources. In this sense, silicon heterojunction (SHJ) solar cells have excelled owing to their high efficiency and low-temperature processing. Nevertheless, manufacture of conventional SHJ solar cells requires complex deposition systems that involve the use of hazardous gases.

Recently, alternative materials have demonstrated good charge-carrier selectivity on silicon. Concretely, oxides of transition metals such as tungsten, molybdenum or vanadium are very effective hole-selective contacts. Furthermore, these materials can be easily deposited by thermal evaporation or sputtering. Several studies have reported successful performance of thermal evaporated transition metal oxides (TMO's) acting as selective contacts. However, a parametrizable deposition technique such as sputtering is more suitable for industrial applications. For this reason, research is needed to be carried out for sputtered TMO's.

In this project, molybdenum oxide layers have been deposited by sputtering on crystalline silicon wafers. These layers have been characterized, focusing on composition, structure, and optoelectronic properties. Additionally, solar cell test devices have been fabricated and characterized in order to evaluate the performance of these layers.

Acknowledgements

First, I would like to acknowledge Cristóbal and Joan, directors of this bachelor thesis, for initiating me in the world of research and helping me so much.

I am very grateful to Mireia, for carrying out XPS analysis, and helping me with transmittance measurements and sputtering depositions.

I want to thank my friend Eloi, with whom I have exchanged so many interesting ideas and good moments.

I also acknowledge Guillermo, who previously had carried out the studies of evaporated transition metal oxides. His work has been essential for the development of this project.

I acknowledge Quim, who always contributes with wise ideas.

I am grateful to all the people who, somehow, took some part in this and helped me when I asked: Gema, the cleanroom staff, the PhD students, and the researchers of the GECFET group of Universitat de Barcelona and of the MNT group of Universitat Politècnica de Catalunya.

And specially, thanks to my family, my friends, and to Gemma, for being always there.

Contents

Chapter 1

Introduction

The need for clean energies

In the last century, world energy consumption has risen in parallel with the exponential increase of population and better living standards, which, in turn, have been produced by a fast scientific progress in medicine and technology. In order to satisfy the demand, coal has been –and still is– the main energy source, alongside oil and natural gas. This is due to its abundance, easy extraction and the simple process to generate energy from its combustion. However, the excessive and uncontrolled use of these fossil fuels is, at long term, harmful for humanity. This is mainly for two reasons: (1) the exploitation time of these sources is far smaller than their regeneration time, and hence these sources will be depleted in few years [1]; and (2) their extraction, treatment and combustion processes are detrimental for nature [2–9].

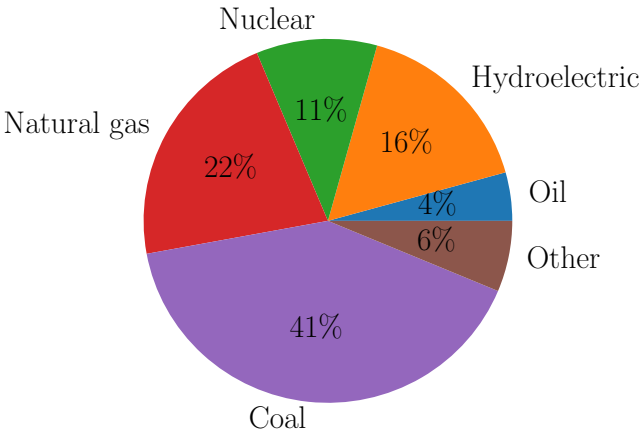

Figure 1.1: World electricity production by source (2014). Data from [10].

Currently, two-thirds of the electricity produced in the entire world are generated from fossil fuels, as shown in Fig. 1.1. In order to be able to produce clean energy in the future, renewable alternatives need to become the main source of energy. Wind and water flows, geothermal energy or the Sun's light are different types of renewable energies that can be used to produce electricity. Not only one, but the combination of all of them is necessary in order to satisfy the consumption demand. This work explores a novel technology to be applied in photovoltaic solar cells, which are devices able to convert sunlight directly into electricity.

Photovoltaic energy

The photovoltaic effect is the responsible for the production of electricity from photons being absorbed by semiconductor materials and producing electron-hole pairs that are collected.

Silicon (Si) is the most used semiconductor to fabricate solar cells. Because of its band-gap of 1.1 eV, it can absorb much of the light incident to the Earth's surface. However, it is not due to its physical properties that silicon is the most popular material in photovoltaic technologies, but the fact that its prominence in the integrated circuit industry has made it a very well studied material. The device physics of silicon is well understood, and its high purity production is largely perfected. This predominance of silicon over other materials is reflected in Fig. 1.2, where it is seen that more of the 90 % of the photovoltaic production in 2015 was achieved using silicon technologies.

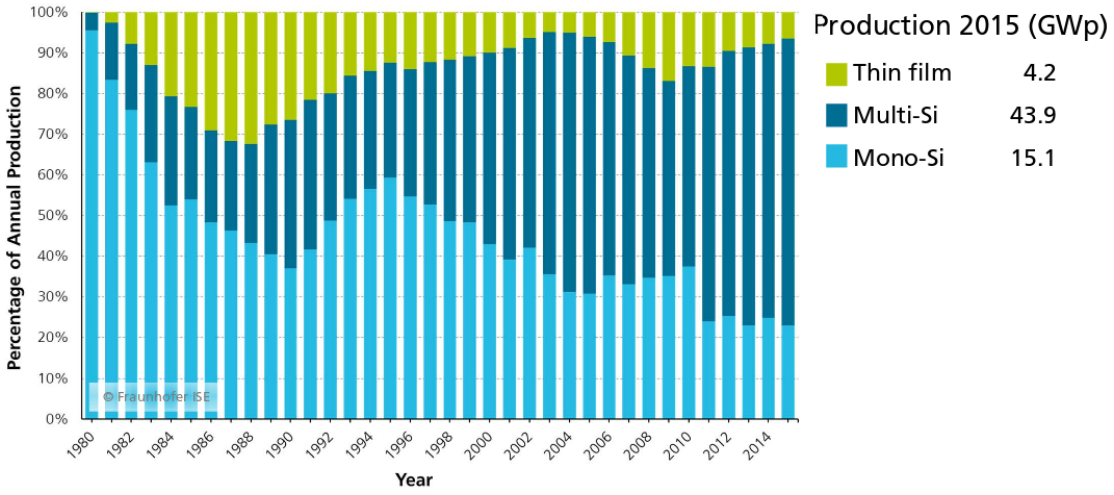

Figure 1.2: Photovoltaic production by technology. Percentage of global annual production from 1980 to 2015. Figure obtained from [11]. © Fraunhofer ISE.

In order to reduce fabrication costs of Si-based solar cells, the thickness of silicon wafers is wanted to be reduced. However, standard fabrication techniques consist on inducing a highly doped region in a wafer to create a p^+n (or an n^+p) junction by annealing it at high temperatures ($\sim$ 1000 °C) in a phosphorous or boron environment, and this is not compatible with thin wafers. When a thin silicon wafer is heated up to high temperatures, it becomes curved. Therefore, in the encapsulation process, it can break. Consequently, low temperature processes are desired in order to further reduce the thickness of the wafers. Moreover, lower processing temperatures would also decrease the energetic cost of solar cell fabrication.

In this sense, silicon heterojunction (SHJ) solar cells have been extensively investigated during the last decades. This technology consists on depositing selective contacts rather than diffusing a dopant into the wafer. The main example of this is heterojunction with intrinsic thin film (HIT) technology, which consists on depositing an intrinsic/doped stack of amorphous Si (a-Si) on each side of a Si wafer. Thus, each stack will act as a selective contact, with an n-doped layer to transfer electrons and a p-doped layer to transfer holes. Using this cost-effective technologies, efficiencies higher than 25 % have been achieved [12, 13]. Nevertheless, a-Si deposition require the use of toxic and flammable gases such as silane, phosphine, diborane or methane. Since any danger and its consequent additional costs are desired to be avoided, alternatives to this technology need to be investigated.

Very recently, different materials have been proposed to replace doped amorphous silicon layers in a new kind of heterojunction solar cells [14]. Among them, transition metal oxides (TMO's) arise as excellent hole-selective contacts. Some of these TMO's that have been reported to work successfully are molybdenum [15–19], vanadium [19] and tungsten [18, 19] oxides. The high band-gap and workfunction of these materials, alongside their semiconductor characteristics accentuated by oxygen vacancies [20], allow them to block electrons and transfer holes. Particularly, molybdenum oxide (MoO_3) has been widely studied in the literature [21].

Since this is a novel and developing research topic, layers of these materials have been deposited using thermal evaporation, which is a very easy way to deposit thin films on a substrate. Nevertheless, this method is poorly controllable and not suitable for industrial applications. In contrast, sputtering is a deposition method used in industry that has many controllable variables: temperature, pressure, gas flow, and RF power. For this reason, in this project, the characteristics of sputtered layers of one of the most investigated transition metal oxides, molybdenum oxide, are studied.

Chapter 2

Theoretical basis

2.1 Basic principles of solar cells

2.1.1 Absorption of photons

The first step of the photovoltaic effect takes place with the absorption of a photon. The energy lost by the absorbed photon is gained by an electron excited into states of higher energy. In order for a photon of any arbitrary energy to be absorbed, *i.e.* for a body to be black, a continuous range of energy states must be available for electrons to be excited. The most approximate case are metals [1], which have an uninterrupted density of states nearby the Fermi level. Within this case, an excited electron will relax easily, generating a phonon for each small loss of energy, until it reaches the Fermi level. This relaxation process, depicted in Fig. 2.1, takes place in times of the order of picoseconds (10^{-12} s) [22]. Due to their low lifetime of excitation, metals are not suitable for producing electricity efficiently.

On the other hand, this mechanism is different in semiconductors. In semiconductor materials, the Fermi level is surrounded by a gap of forbidden states that separates the valence and the conduction bands. The valence band contains the electronic states with energies below the gap and is nearly completely occupied. In contrast, the conduction band contains the electronic states with energies above the gap and is nearly empty. Since there are not states inside the gap, an electron cannot be excited by a photon with energy smaller than E_G, so photons with energy $\hbar\omega < E_G$ are not absorbed by the material, *i.e.* they are either reflected or transmitted. As shown in Fig. 2.1, an electron being excited into the conduction band starts to lose its energy as quickly as in a metal by step-wise generation of phonons. However, once the electron has reached the lower limit E_C

[1] Actually, metals reflect most of the light, except when their surface is roughened. In this case, a metal behaves as a black body absorbing most of the incident light.

of the conduction band, losing energy in small steps by generating phonons is no longer possible, since the only states available for the electron to lose energy are located at an energy E_G below E_C. Hence, in order to return to E_V the electron must lose an amount of energy E_G in a single step. Possible relaxation processes are the emission of a photon or the simultaneous generation of a large number of phonons. However, both processes are much less probable than the step-wise generation of phonons in a continuous range of available states. Consequently, the lifetime of these excited electrons is far larger than in metals, usually of the order of milliseconds (10^{-3} s) [22]. This long time of excitation allows electrons to be collected in the contacts so as to generate electricity.

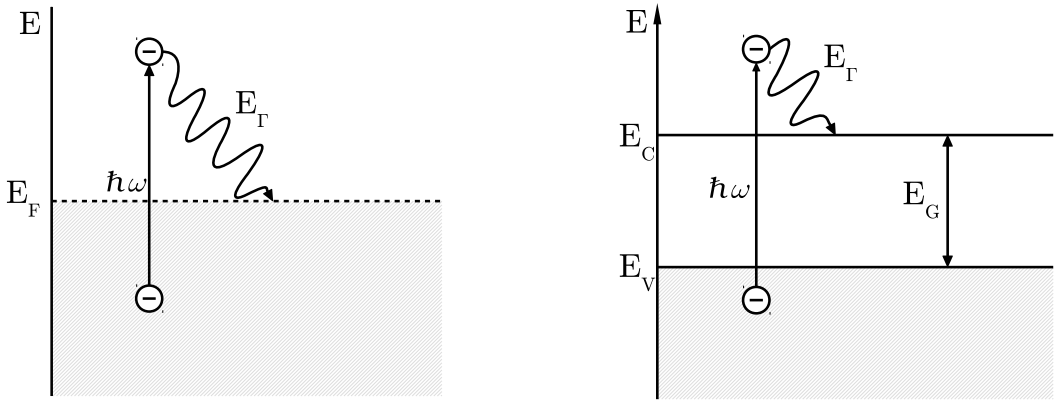

Figure 2.1: Excitation and subsequent thermal relaxation of an electron when a photon of energy $\hbar\omega$ is absorbed in a metal (left) and in a semiconductor (right).

2.1.2 Review of semiconductor physics

In this section, the fundamentals of the physics of semiconductors are briefly explained as in [23]. The aim is to review the basis of traditional theory in order to go beyond and understand modern explanations.

Density of states

When electrons move in a particular direction in a semiconductor crystal, their movements can be described by standing-wave oscillations. Thus, the wavelength λ of the oscillations must be a multiple of the material length L in that particular direction, *i.e.* $n\lambda = L$, where n is an integer.

According to the De Broglie relation, the wavelength can be expressed in terms of the electron's momentum: $\lambda = \frac{h}{p_i}$, where h is the Planck constant and p_i is the

electron momentum in the i direction. Thus, we obtain that $Lp_i = hn_i$. [2]

For a unity increase of n_i, the needed increment of the momentum dp_i is $L\ dp_i = h$. Considering a three-dimensional cube of side L, we have that $L^3 dp_x dp_y dp_z = h^3$, meaning that the volume for an energy state in momentum space is h^3.

The differential volume of the momentum can be written as $dp_x dp_y dp_z = 4\pi p^2 d\vec{p}$, which represents the volume between two concentric spheres from $\vec{p}$ to $\vec{p} + d\vec{p}$. Thus, the density of states $N(E)$ between energies E and $E + dE$ can be written as $N(E)dE = 8\pi p^2 d\vec{p} h^{-3}$.

From the relation of the kinetic energy with the momentum, $E = \frac{1}{2}mv^2 = \frac{\vec{p}^2}{2m_e}$, where m_e is the electron effective mass, the expression for the density of states can be found:

$$N(E) = 4\pi \left(\frac{2m_e}{h^2}\right)^{\frac{2}{3}} E^{\frac{1}{2}} \tag{2.1}$$

Carrier concentration

In an intrinsic semiconductor, the concentration of electrons in the conduction band and holes in the valence band is mainly due to thermal excitation. Their concentration in an energy range dE can be calculated as the product of the density of states and the probability of occupying these states. Since electron and holes are half-integer spin particles, their behaviour is described by Fermi-Dirac statistics, and their probability of occupation is given by the Fermi distribution function

$$F(E) = \frac{1}{1 + e^{\frac{E - E_F}{k_B T}}} \tag{2.2}$$

where k_B is the Boltzmann constant, T the temperature, and E_F the Fermi level, which accounts for the energy at which the probability of occupation is $\frac{1}{2}$. Since we are only concerned by energies $E >> k_B T$, the probability of occupation can also be described by Boltzmann distribution: $F(E) \approx e^{-\frac{E - E_F}{k_B T}}$. Then, the concentration of electrons can be computed as

$$n = \int_0^\infty N(E)F(E)dE = 2\left(\frac{2\pi m_e k_B T}{h^2}\right)^{\frac{3}{2}} e^{\frac{E_F}{k_B T}} \tag{2.3}$$

This derivation can be found in more detail at [23]. If we consider the bottom of the conduction band as E_C instead of $E = 0$, the electron concentration at the

[2] Here n_i refers to the number of wavelengths contained within the dimension i of the semiconductor. It should not be misunderstood as the intrinsic carrier concentration, which will be introduced later in this manuscript

conduction band is obtained:

$$n = N_C e^{-\frac{E_C - E_F}{k_B T}} \tag{2.4}$$

with $N_C = 2\left(\frac{2\pi m_e k_B T}{h^2}\right)^{\frac{3}{2}}$ being the effective density of states in the conduction band. Similarly, for holes at the valence band,

$$p = N_V e^{-\frac{E_F - E_V}{k_B T}} \tag{2.5}$$

with $N_V = 2\left(\frac{2\pi m_h k_B T}{h^2}\right)^{\frac{3}{2}}$ being the effective density of states in the valence band.

In an intrinsic semiconductor, $n = p = n_i$, where n_i is the intrinsic carrier density. Thus,

$$np = n_i^2 = N_C N_V e^{-\frac{E_G}{k_B T}} \tag{2.6}$$

This is called the mass action law, and it is fulfilled under thermal equilibrium.

Extrinsic semiconductors

In doped (extrinsic) semiconductors, there are acceptor and donor impurities that, due to thermal excitation, promote holes into the valence band and electrons into the conduction band, respectively. Thus, materials with more donor than acceptor impurities become n-type semiconductors, and the opposite with p-type semiconductors. This is depicted in Fig. 2.2.

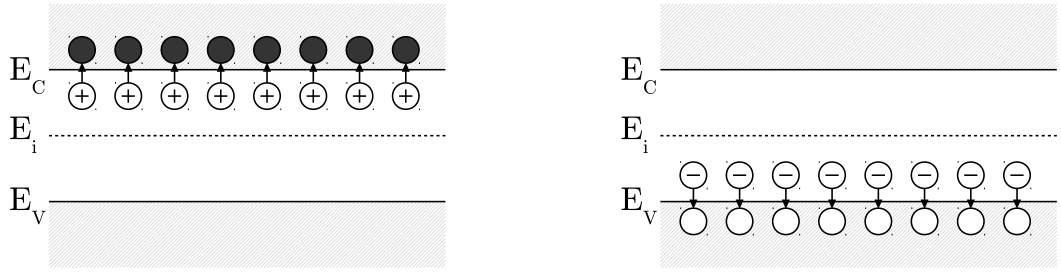

Figure 2.2: Schematic energy band representation of extrinsic semiconductors with donor (left) and acceptor (right) impurities. Black circles represent electrons in the conduction band and white circles represent holes in the valence band.

The concentration of carriers in an extrinsic semiconductor can be found through the condition of charge carrier neutrality, *i.e.* $n + N_A = p + N_D$, and from the mass action law. However, at usual device operation temperatures, $n_n \approx N_D - N_A$ when $N_D >> N_A$, and $p_p \approx N_A - N_D$ when $N_A >> N_D$. Here the subindexes n

and p account for n and p-type semiconductors. N_A and N_D are the acceptor and donor concentrations.

Carrier transport

Carrier transport in semiconductors is due to two phenomena: drift and diffusion. Drift current of charged particles is due to the force applied by an electric field. On the other hand, diffusion moves carriers along a spatial concentration gradient (from higher to lower concentrations).

Drift. The momentum gained by an electron in a semiconductor where an electric field is applied is $m_e v_e$, where m_e and v_e are the electron's effective mass and its drift velocity, respectively. Moreover, the momentum applied to the electron by the electric field is given by $-q\mathcal{E}\tau_c$, where q is the elementary charge, $\mathcal{E}$ is the electric field, and τ_c is the mean time between collisions. Thus, $v_e = -\mu_n \mathcal{E}$, with $\mu_n = \frac{q\tau_c}{m_e}$ being the mobility of electrons. Respectively, $v_h = \mu_p \mathcal{E}$ for holes.

The drift current density for electrons can be written as the sum of the contributions of all of them, *i.e.* $J_n = \frac{I_n}{A} = \sum_i (-q v_i)$. The contributions of all electrons, though, can be substituted by the product of the mean drift velocity and the electron concentration. This is, $J_n = -qnv_e = qn\mu_n\mathcal{E}$. Thus, the total drift current, which is the sum of electron and hole drift currents, can be formulated as follows:

$$J_{\text{drift}} = (qn\mu_n + qp\mu_p)\mathcal{E} = \sigma\mathcal{E} \tag{2.7}$$

where σ is the conductivity of the material, which is the inverse of the resistivity.

Diffusion. Diffusion current results from the thermal motion of carriers in a concentration gradient. This is described by Fick's law, which states that the diffusion current is proportional to the concentration gradient by a factor D called diffusivity. Thus, the electric current due to diffusion for electrons is $J_n = qD_n\frac{dn}{dx}$, while $J_p = -qD_p\frac{dp}{dx}$ accounts for holes.

Joining these two transport contributions, the total carrier transport for electrons, J_n, and for holes, J_p, can be written as:

$$J_n = q\mu_n n\mathcal{E} + qD_n\frac{dn}{dx} \tag{2.8}$$

$$J_p = q\mu_p p\mathcal{E} - qD_p\frac{dp}{dx} \tag{2.9}$$

Generation and recombination

When there is injection of excess carriers the thermal equilibrium condition is broken ($np \neq n_i^2$). The mechanism responsible of restoring equilibrium is the recombination of an electron in the conduction band with a hole in the valence band, thus annihilating one electron-hole pair. This process can be a direct band-to-band recombination (important for direct band gap semiconductors) or trap-assisted recombination through recombination centers. The opposite process is called generation and can be either due to thermal or light-induced excitation.

In most cases, the recombination rate can be described as the excess of minority carriers, *e.g.* Δp_n for holes in an n-type semiconductor, divided by their lifetime τ_p: $R = \frac{\Delta p_n}{\tau_p}$.

The change of carrier concentration in time is then equal to the generation minus the recombination of carriers. However, if the current is not uniform along the material, its gradient has to be taken into account. These considerations lead to the so called continuity equations:

$$\frac{\partial n}{\partial t} = G_n - R_n + \frac{1}{q}\frac{\partial J_n}{\partial x} \tag{2.10}$$

$$\frac{\partial p}{\partial t} = G_p - R_p - \frac{1}{q}\frac{\partial J_p}{\partial x} \tag{2.11}$$

Because of the abrupt discontinuity of the semiconductor's lattice structure at the surface, a large number of recombination centers may be introduced at the surface region. In this case, the recombination rate has the form of $U_s = S\Delta p_n$ (for holes in an n-type semiconductor), where S represents the surface recombination velocity and has units of velocity ($\mathrm{cm} \cdot \mathrm{s}^{-1}$). At a recombinative surface, the diffusion current density of minority carriers is equal to the surface recombination rate:

$$qD_p \left.\frac{dp_n}{dx}\right|_{x=0} = qS\Delta p_n(0) \tag{2.12}$$

P-N junction

Let's consider a p-n junction under equilibrium conditions. The current density for each carrier is then equal to zero, so the drift and diffusion currents compensate each other: $q\mu_p\mathcal{E} = qD_p\frac{dp}{dx}$. Using Einstein's relation $\frac{D}{\mu} = \frac{k_B T}{q} \equiv V_T$, where V_T is the thermal voltage, the electric field can be found. Since the electric field is the negative gradient of the voltage V, the built-in voltage V_{bi} of the junction can be calculated by integrating at both sides of the equality, leading to

$$V_{bi} = V_T \ln\left(\frac{N_A N_D}{n_i^2}\right) \tag{2.13}$$

$$p(x_n) = p(x_p) e^{-\frac{V_{bi}}{V_T}} \tag{2.14}$$

$$n(x_p) = n(x_n) e^{-\frac{V_{bi}}{V_T}} \tag{2.15}$$

where x_n and x_p represent the limits of the depletion region at the p and n zones, respectively. To fulfill the neutral charge condition, the sum of the charges must be zero: $Q_n + Q_p = 0 \implies qN_D x_n = qN_A x_p$. From this equality, the width of the depletion region can be written as $W = x_n + x_p = \left(1 + \frac{N_D}{N_A}\right) x_n$.

From Gauss law, and from the relation between the electric field and the electric potential, $\frac{d^2V}{dx^2} = -\frac{\rho}{\epsilon}$, where ρ is the charge density and $\epsilon = \epsilon_r \epsilon_0$, being ϵ_r the dielectric constant of the material and ϵ_0 the vacuum permittivity. Solving for V, and after some algebraic manipulations, the width of the depletion region is found to be

$$W = \sqrt{\frac{2\epsilon_r \epsilon_0}{q} \frac{N_A + N_D}{N_A N_D} (V + V_{bi})} \tag{2.16}$$

Here it has been considered that the electric potential along the junction is the built-in potential plus the applied bias V.

The capacitance of the depletion region can be computed with the formula for two parallel infinite plates, *i.e.* $C = \frac{W}{\epsilon}$. The squared inverse of the capacitance has a linear behaviour in terms of the applied bias. In the case of a p^+n junction, when $N_A >> N_D$, the width of the p^+ depletion region can be neglected, and the following expression is obtained:

$$\frac{1}{C^2} = \frac{2(V - V_{bi})}{q\epsilon_r \epsilon_0 N_D} \tag{2.17}$$

Current-voltage characteristics. When a bias is applied, Eq. (2.15) becomes $n(x_p) = n(x_n) e^{-\frac{V_{bi} - V}{V_T}} = n(x_n) e^{\frac{V}{V_T}} e^{-\frac{V_{bi}}{V_T}}$. Considering that $n(x_n) \approx N_D$ and using Eq. (2.13) and the mass law action, we find that $n(x_p) = \frac{n_i^2}{N_A} e^{\frac{V}{V_T}}$ and $p(x_n) = \frac{n_i^2}{N_D} e^{\frac{V}{V_T}}$. Defining $n_{p0} \equiv \frac{n_i^2}{N_A}$, one can find the expression for the excess of minority carriers: $\Delta n(x_p) = n_{p0}\left(e^{\frac{V}{V_T}} - 1\right)$, and respectively for holes.

The total current is constant along the junction, so we can take any point to calculate it. For simplicity, we take the point $x = x_p$. There, the total current is $J_T = J_n(x_p) + J_p(x_p)$. At the point x_p, the drift current of electrons is negligible

since electrons here are minority carriers and the electric field is small. Then, $J_n(x_p) \approx qD_n \left.\frac{dn}{dx}\right|_{x_p}$. The drift current of holes at x_n is also negligible.

From the continuity equation, considering stationary regime and that generation equals recombination, we find that the current density of holes at x_p is the same at x_n. Thus, the total current is equal to the diffusion currents of electrons and holes at x_p and x_n, respectively.

Solving the continuity equation considering stationary regime ($\frac{dn}{dt} = 0$), zero generation ($G = 0$), that the diffusion length L_i of carriers n or p is longer than the wafer material's length, and that the drift current for minority carriers in quasi-neutral regions is negligible, the excess carrier concentration is found to be $\Delta n(x) = \frac{n_i^2}{N_A} e^{-\frac{x}{L_n}} \left(e^{\frac{V}{V_T}} - 1\right)$ for electrons, and respectively for holes. In this case, the total current is found to be the characteristic one of diodes:

$$J = J_0 \left(e^{\frac{V}{V_T}} - 1\right) \tag{2.18}$$

with $J_0 = qn_i^2 \left(\frac{D_n}{L_n N_A} + \frac{D_p}{L_p N_D}\right)$.

In a photodiode (or a solar cell), the diode expression is added to the photocurrent, which is equal to the short-circuit current with negative sign: $J_{ph} = -J_{sc}$. This leads to the expression $J = J_0 \left(e^{\frac{V}{V_T}} - 1\right) - J_{ph}$. From this, the open-circuit voltage is found to be $V_{oc} = V_T \ln\left(\frac{J_{ph}}{J_0} + 1\right) \approx V_T \ln\left(\frac{J_{ph}}{J_0}\right)$

Quasi-Fermi level

Irradiation in a direct-gap semiconductor leads to generation of electron-hole pairs, so the concentration of both charge carriers is larger than their respective in dark. Hence, the action mass law is not accomplished *a priori*: $np > n_i^2$. Moreover, due to the increased electron density, the Fermi level describing their distribution in the conduction band must be closer to E_C than in dark, and analogously with holes at the valence band. The solution to this is to describe differently the distribution of electrons at the conduction band and of holes at the valence band by introducing two different Fermi distributions with Fermi energies E_{FC} and E_{FV} called quasi-Fermi levels. Thus, the carrier concentrations can be described as $n = N_C e^{-\frac{E_C - E_{FC}}{k_B T}}$ for electrons and $p = N_V e^{-\frac{E_{FV} - E_V}{k_B T}}$ for holes, so that $np = n_i^2 e^{\frac{E_{FC} - E_{FV}}{k_B T}}$.

2.1.3 Charge carrier separation and collection

Charge carrier transport. Würfel's approach

In their article [24], Würfel *et al.* rewrite the expressions for carrier transport using an alternative perspective in three simple steps.

First, the drift current can be written as $J_{\text{drift}} = \sigma_n \mathcal{E} = -\frac{\sigma_n}{q}\nabla(q\varphi)$, where $\sigma_n = qn\mu_n$ is the conductivity of electrons, φ is the electric potential, and the electric force acting on the electrons is $-\nabla(q\varphi)$.

Second, the diffusion current can be described as $J_{\text{diff}} = qD_n\nabla n = qnD_n\frac{\nabla n}{n} = \frac{\sigma_n}{q}\nabla\Phi_{\text{chem},n}$, where $\Phi_{\text{chem},n} = \Phi_{\text{chem},n,0} + k_B T \ln\left(\frac{n}{n_0}\right)$ is the chemical potential of electrons. Here, the chemical force acting on electrons and causing diffusion is $-\nabla\Phi_{\text{chem},n}$.

Adding both expressions, the resulting current is found to be due to the force $-\nabla\Phi_{\text{chem},n} - q\varphi = -\nabla\eta_n$, where η_n is the electrochemical potential. Using that the electrochemical potential is the same as the Fermi level [22], we find the following expressions for the current density of electrons and holes:

$$J_n = \frac{\sigma_n}{q}\nabla E_{FC} \tag{2.19}$$

$$J_p = -\frac{\sigma_n}{q}\nabla E_{FV} \tag{2.20}$$

This can be understood as the fact that particles move in a direction where their free energy decreases, thereby allowing entropy to be generated. Since the electrochemical potential is the free energy of charged particles at constant temperature and constant volume, the expressions above follow this statement without need of using fields or concentration gradients. Thus, it can be stated that charge carriers move by gradients of their quasi-Fermi levels.

Charge carrier separation in solar cells

In order to generate an electrical current in solar cells, electrons and holes generated from illumination have to move toward different contacts. Thus, films defined as hole transport (HTL) or electron transport (ETL) layers are needed. The ETL would be located at the vicinity of the "electron contact" (electron collector), whereas the HTL would be located at the vicinity of the "hole contact" (electron injector). According to Eq. (2.19) and (2.20), this can only be achieved by having a high conductivity of electrons (holes) and a low conductivity of holes (electrons) at the ETL (HTL). Thus, an amount of electrons (holes) larger than holes (electrons) will flow through the ETL (HTL). This can be achieved by different manners, such

as having an n-doped region as ETL or a high energy barrier for the carriers that are wanted to be blocked.

2.2 Molybdenum oxide as hole-selective contact

Stoichiomoetric molybdenum oxide (MoO_3) is an insulator, due to its large band gap of $\sim$ 3 eV [25]. However, when it is reduced to MoO_x (with $x < 3$), the oxygen vacancies act as donor impurities doping the material and shifting its Fermi level closer to the conduction band (which corresponds to the lowest unoccupied molecular orbital) [20]. Since molybdenum oxide also has a high workfunction of $\sim$ 6 eV [20], an energy barrier is created for electrons in the conduction band in a MoO_x/Si heterojunction. As depicted in Fig. 2.3, holes do not seem likely to flow through MoO_x. However, one can think that electrons coming from the front contact flow through the band of defect-states created by donor oxygen vacancies, which is the same as saying that holes flow from c-Si towards ITO and the front contact.

The diagram depicted below shows the band structure and conduction mechanisms of a c-Si solar cell with MoO_x acting as HTL and an intrinsic (i)/n stack of hydrogenated a-Si (a-Si:H) acting as a semiclassical approach for the ETL. Indium tin oxide (ITO), which is a transparent conductive material, acts as an antireflective layer used to improve photocurrent generation.

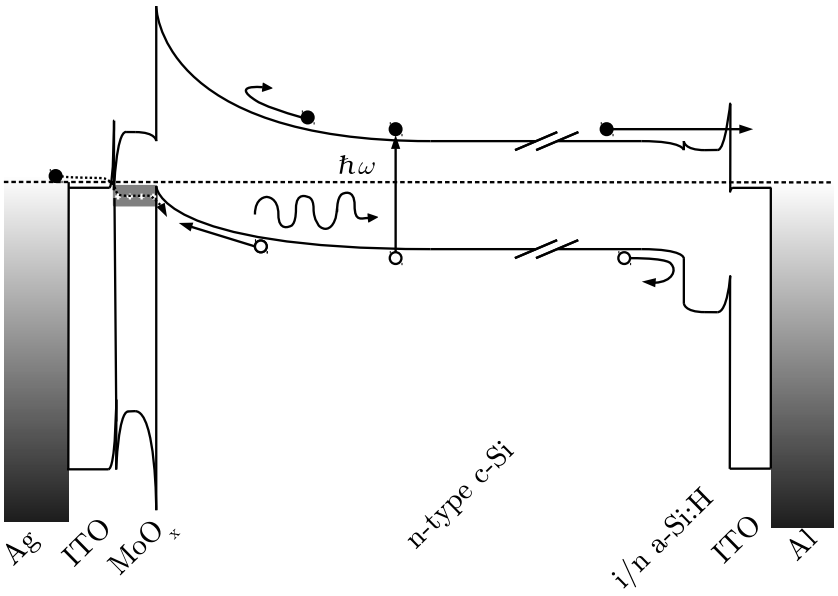

Figure 2.3: Schematic band diagram of a c-Si solar cell with MoO_x as HTL and an i/n a-Si:H stack as ETL.

Chapter 3

Fabrication and characterization

3.1 Fabrication processes and facilities

3.1.1 Clean room

A clean room is a room in which the concentration of airborne particles is controlled. It is constructed and used in a way to minimize the introduction, generation and retention of particles inside the room. In this kind of facilities, other relevant parameters, *e.g.* temperature, humidity, and pressure, are controlled as necessary.

This environment is achieved through the use of appropriate heating, ventilation and air conditioning systems, beside high efficiency particulate air filters that maintain the correct pressurization, temperature, and humidity of the facility, as well as the air flow of the circulating, continuously filtered air.

In micro and nano-technology fields, small undesired particles can damage the behaviour of the fabricated devices. The steps of fabrication usually involve thin film deposition on a wafer. It is essential that the surface of the wafer is completely clean before each deposition takes place because, otherwise, some particles (from air, our clothes, skin, mouth...) can deposit there and create pinholes that could lead to short-circuits or bad performance of the devices.

In this project, clean room facilities of Universitat Politècnica de Catalunya (UPC) and Universitat de Barcelona (UB) are used to perform different steps of the fabrication of test devices. In UB, the deposition of molybdenum oxide by RF magnetron sputtering has been carried out. In UPC, several technological processes have been performed: depositions (thermal evaporation and plasma enhanced chemical vapor deposition), wafer cleaning, lithography and annealing in forming gas environment.

3.1.2 Wafer cleaning

The principal wafer cleaning process is known as RCA Standard Clean, which was developed by Werner Kern while working for the Radio Corporation of America (RCA) [26]. The recipe used in UPC's cleanroom consists of two processes: RCA 1 and RCA 2:

RCA 1 Solution used: 1500 ml deionized (DI) H_2O (18 MΩ), 250 ml H_2O_2, 250 ml NH_3. Introduce wafers in the cold solution. Heat up the solution at heater level 9 for 13 min and then 7 min more at position 3. Quenching of hot solution for 5 min under running water (18 MΩ). HF 1 % dip for 1 min.

RCA 2 Solution used: 1800 ml H_2O DI (18 MΩ), 100 ml H_2O_2, 100 ml HCl. Heat up the solution at heater level 9 for 10 min. Introduce wafers (solution have to be boiling) and then 10 min more at position 3. (4) Quenching of hot solution for 4 min under running water (18 MΩ). (5) HF 1 % dip for 1 min.

Whereas RCA 1 removes organic residues, RCA 2 removes traces of metallic (ionic) contaminants. The HF dipping removes the thin oxide layer formed at the surface of the silicon wafer. This process is applied to bare wafers before the first film deposition.

3.1.3 Deposition methods

RF magnetron sputtering

Sputtering is a physical vapour deposition method in which atoms are ejected from a source surface through the impact of high-energy gaseous ions [27]. A radio-frequency (RF) discharge is applied between the target and the substrate (and the chamber walls) in a vacuum chamber where an inert gas such as argon (Ar) flows.

The process starts with the ionization of Ar atoms (Ar^+) by collisions from electrons accelerated by the electric field. The cations are accelerated as well, colliding with neutral atoms and thus forming new ions –if their kinetic energy is greater than the gas ionization energy. In this environment, a self-sustaining plasma is formed as long as the pressure and the electric potential are maintained in an appropriate range. If the Ar^+ ions have enough momentum, target molecules are ejected in vapour phase. In this low pressure environment, condensation occurs under concurrent bombardment by energetic species, which promotes nucleation, compound formation and film growth on the substrate and the chamber walls [28, 29].

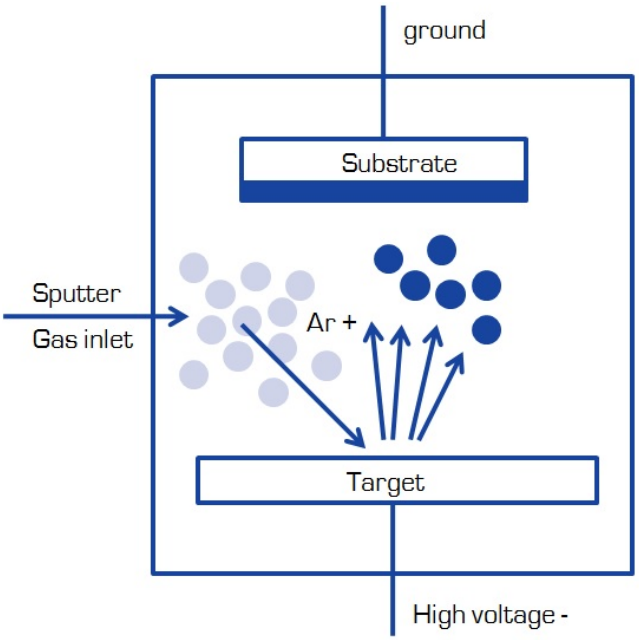

Figure 3.1: Schematic representation of a sputtering system. The inert gas bombards the target, and target particles are deposited on the substrate. Image obtained from [30].

The efficiency of this process is dramatically increased with magnetic confinement of charged plasma particles close to the target. A higher amount of collisions occurs and, thus, more Ar^+ cations are created. Consequently, the deposition rate is risen. This improved technique is called magnetron sputtering [31].

The RF magnetron sputtering equipment *ATC-ORION 8 HV* from *AJA International, Inc* with a MoO_3 ceramic target was used to deposit molybdenum oxide controlling parameters such as pressure, RF power, gas flow and substrate temperature.

Thermal evaporation

In this technique, a tungsten boat is connected to a current source. On the boat, the material to be deposited is placed (in form of powder, wire, pellets, *etc.*), and the substrate is located at some distance above the boat. When large current intensities ($\sim$ 300 A) flow through the tungsten boat, the boat is heated up to temperatures high enough to evaporate the material, which is deposited on the walls of the vacuum chamber as well as on the surface of the substrate.

This method was used to deposit metal contacts with materials such as gold, aluminum and silver.

Plasma enhanced chemical vapour deposition

Plasma enhanced chemical vapour deposition (PECVD) is the most commonly used technique for the deposition of amorphous silicon. In this method, reactive gases such as silane (SiH_4) and methane (CH_4) are introduced into a vacuum chamber, where a RF discharge is applied between two parallel plates at a frequency of 13.56 MHz [1], creating a plasma of these gases, which react within the plasma and condensate on the substrate forming a film.

This method allows growing both intrinsic and extrinsic layers of a-Si. Only SiH_4 and CH_4 are needed to deposit films of intrinsic hydrogenated amorphous silicon carbon (i a-SiC_x:H). On the other hand, combining SiH_4 with phosphine (PH_3) or diborane (B_2H_6) results in the deposition of n or p-type a-Si. Characteristics of these thin films such as bandgap and conductivity can be tailored by playing with the pressure and the ratio between gas flows. Several works have demonstrated that the passivation of c-Si wafer's surface by a-Si:H allows the fabrication of high efficiency solar cells using a low temperature process such as PECVD [32, 33]. However, as discussed earlier, the gases involved are dangerous, so alternatives are desired. In this project, a stack of i/n a-Si:H was used as a semiclassical approach for the electron contact.

[1] See `https://en.wikipedia.org/wiki/ISM_band`

3.1.4 Lithography

Lithography is a technique used to obtain a patterned film over a substrate. In this project, it was carried out several times for defining the active areas of solar cells in wafer quarters before depositing the metallic contacts. The process works as follows:

1. A film (in our case MoO_x + ITO) is deposited on a silicon wafer quarter.

2. The photoresist is deposited onto the film by spin coating. The photoresist is also deposited on the rear side of the wafer to protect the rear films. The coated sample has to be annealed for 20 min in order to dry.

3. A photomask is aligned with the wafer. This mask has transparent and opaque regions that will let light go through or block it so that specific regions of the photoresist are illuminated.

4. The sample is exposed to ultraviolet light and is left to rest for 45 minutes without being illuminated by high-energy light that could excite the photoresist. During this time, the excited photoresist will react in order to be removable by the developer.

5. After these 45 minutes, the sample is developed with the photoresist's specific developer. Thus, the illuminated photoresist is removed.

6. The MoO_x + ITO film is etched with hydrofluoric acid. Only the regions that are not protected by the resist will be etched.

7. The remaining photoresist is removed with acetone.

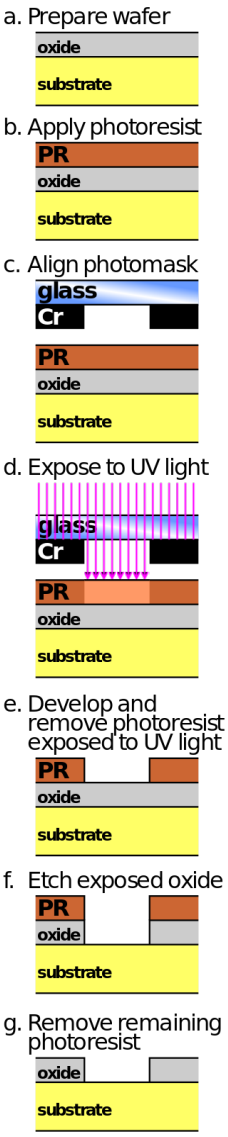

Figure 3.2: Simplified illustration of dry-etching using positive photoresist during a photolithography process in semiconductor microfabrication. Image from [34].

3.1.5 Fabrication steps

TLM test devices

The transfer length method (TLM) has been used in this project to determine the contact and sheet resistances of a material from current-voltage measurements of contacts located at different distances. Its physical principles will be explained in Section 3.2.2. For the moment, only the fabrication steps will be detailed.

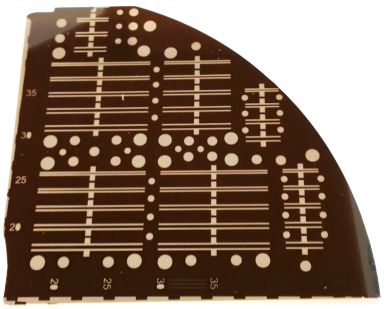

Figure 3.3: Top view of a fabricated TLM test device.

1. A silicon wafer (p or n) is RCA cleaned. Usually the HF step of RCA 2 is not done if the cleaning process is not carried out the same day than step 2.

2. A stack of intrinsic and n-doped hydrogenated amorphous silicon (i a-SiC_x:H + n a-Si:H) is deposited on the rear side of the wafer by PECVD. If the RCA has not been done the same day, the wafer is HF dipped for 1 min. This deposit is only needed when diodes are wanted to be measured -the TLM mask also includes small circles to measure diodes– since the diode need to have an ohmic contact at the rear side.

3. Deposition of MoO_x by sputtering. Prior to deposition, the wafer is dipped in HF for 1 min.

4. Deposition of metallic contacts by thermal evaporation: aluminum (Al) on the a-Si side, gold and silver (Au/Ag) on the MoO_x side. Au is used for the MoO_x contact because of its high workfunction, but since it is expensive, just a very thin layer is deposited, and the contact is thickened by Ag.

The TLM and diode contacts of a fabricated device are shown in Fig. 3.3 and 3.4. In order to get this patterns, a mask is used for the thermal evaporation of Au and Ag.

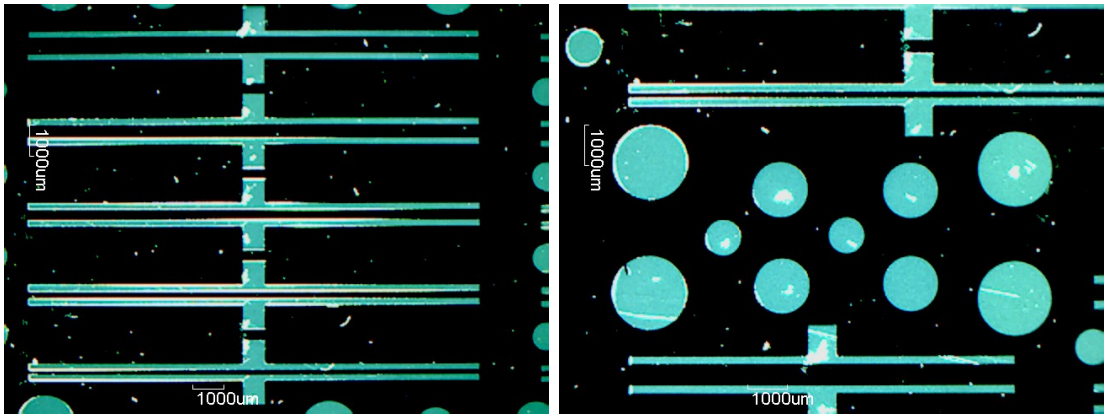

Figure 3.4: Top view of TLM (left) and diode (right) contacts.

Solar cells

There are only a few differences between the fabrication of solar cells and of TLM test devices: an indium tin oxide (ITO) film is used for optical improvement (see Fig. 3.5), the front contact is deposited using a different grid, and lithography is used to define the active area of solar cells. We use wafer quarters, and deposit the materials over all the surface. However, in order to compute the characteristics of a solar cell, a well defined area is needed. In our case, the wafer quarter is patterned defining square active areas which are the actual solar cells (See Fig. 3.5). The fabrication steps are the following:

1. The first steps are the same as in TLM device fabrication: RCA to clean wafers, PECVD to deposit a-Si, and sputtering to deposit MoO_x.

2. An ITO layer is sputter deposited over MoO_x at a substrate temperature of 200 °C. Typically another ITO layer could be deposited on the rear side, over a-Si. However, for simplicity, and in order to speed up the fabrication process, this step is not carried out. The solar cells will then loose some optical performance, but it will not affect the study of MoO_x as HTL.

3. Active areas are defined by photolithography. ITO and MoO_x of the non-active areas are etched by HF dipping.

4. Back (Al) and front (Ag) contacts are deposited by thermal evaporation. In the front contact, a grid pattern is achieved with a mask.

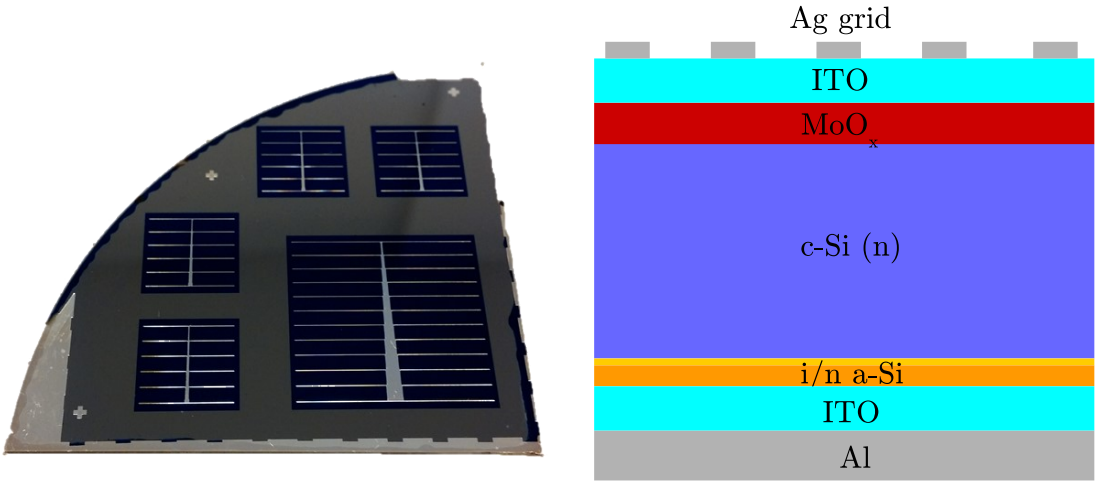

Figure 3.5: Left: Solar cell test device. Right: Schematic representation of the fabricated solar cells.

3.2 Characterization methods

3.2.1 Thickness measurements

A mechanical surface profiler equipped with a stylus was used for the film thickness determination. Due to its low accuracy, this system was only used for determination of contact thicknesses ($\sim 1\ \mu$m).

For determination of thin film thickness, ellipsometry was used. The basic principle of ellipsometry is to measure the changes in incident light's polarization after being reflected in the thin film. From these changes, the film thickness and its refractive index can be computed. More information can be found at [35].

3.2.2 Electrical characterization

Transfer length method

Transfer length method (TLM) was first proposed by Shockley [36]. It consists on measuring the current-voltage characteristics between two coplanar contacts at different distances on a semiconductor device in order to compute the sheet resistance of the material. From the expression that relates the resistance R with the resistivity ρ, one can easily obtain the expression of the sheet resistance: $R = \rho\frac{d}{Zt} = R_{sh}\frac{d}{Z}$, *i.e.* $R_{sh} = \frac{\rho}{t}$, where t is the film thickness. The units of R_{sh} are $\Omega/\square$. The sheet resistance can be understood as the resistance of a square area of the material.

In Fig. 3.6, the contacts of a TLM device are depicted. Since the current enters through a contact and leaves through another contact, the total resistance will be $R_T = 2R_C + R_{sh}\frac{d}{Z}$, where d denotes the distance between the contacts and Z is the contact width. Moreover, the contact resistance can be expressed as $R_C \approx R_{sh}\frac{L}{Z}$, where L is the contact length. However, the current does not use all the contact length, so a more realistic expression would be $R_C \approx R_{sh}\frac{L_T}{Z}$ [37], where L_T denotes the transfer length, which is the length of the contact through which the current flows. Fig. 3.6 also shows how to calculate the contact and sheet resistances from a TLM measurement.

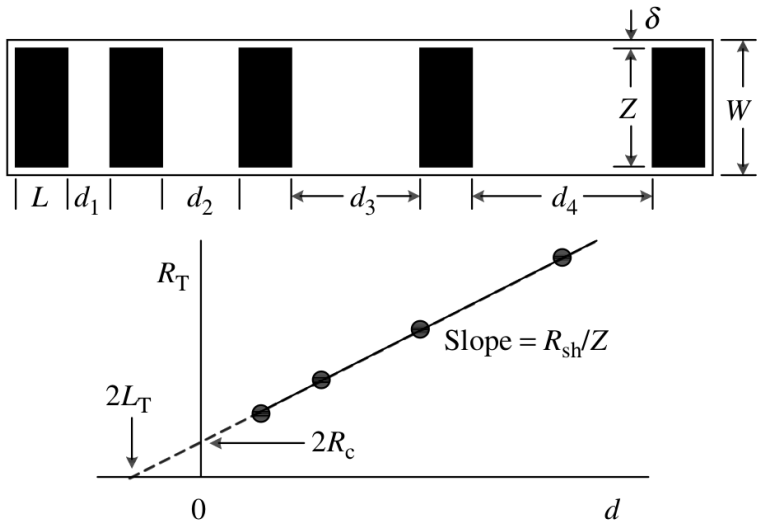

Figure 3.6: Top: schematic representation of the TLM contacts. Bottom: typical plot of the resistances measured and the regression line from which the parameters are obtained. Image from [37].

As can be seen in Fig. 2.3, the region of c-Si close to the interface with MoO_x is supposed to be p^+-inverted. Thus, in a TLM device, the current between the contacts will flow through the inversion layer if this region is much more conductive than MoO_x. Otherwise, the current will flow in parallel through both regions, and can be described as two resistances in parallel. The sheet resistance of the inversion layer can be written as $R_{sh} = (\sigma L_D)^{-1}$, where $\sigma \approx qp\mu_p$ is the conductivity of the inversion layer and $L_D = \sqrt{\epsilon V_T (qp)^{-1}}$ is its Debye length. Thus, since R_{sh} is obtained by TLM measurements, the hole density of the inversion layer can be computed.

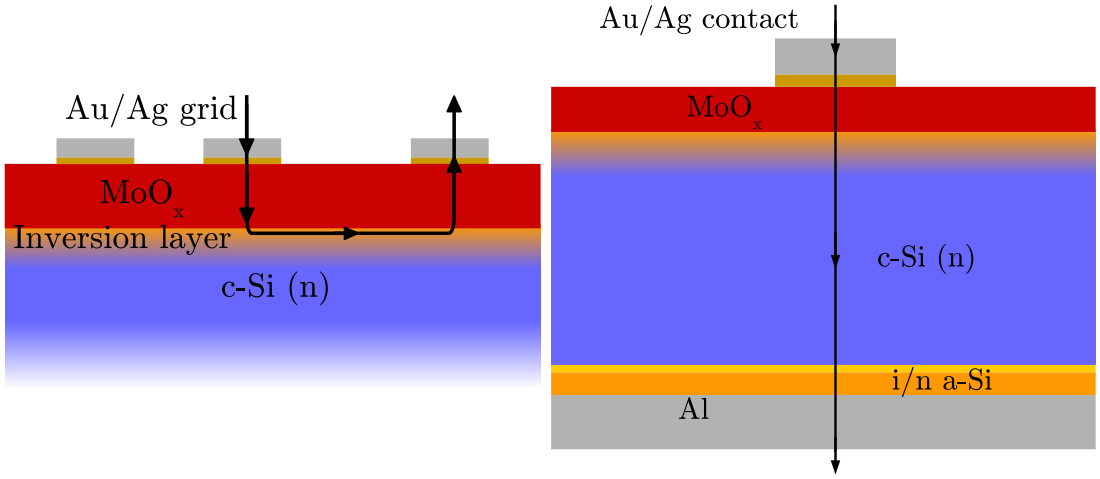

Figure 3.7: Layer structure and current flow in TLM (left) and diode (right) test devices.

Diodes

When measuring diodes, the current between a front and the back contacts is measured. Due to the induction of a p^+n junction, a diode behaviour is seen when varying the bias. The equivalent circuit is the one shown in Fig. 3.8. Thus, the $I-V$ curves measured can be fitted by using the following function:

$$J = J_0\left(e^{\frac{V-JR_s}{nV_T}} - 1\right) + \frac{V - JR_s}{R_p} \quad (3.1)$$

By fitting the curves measured with this function, J_0, the ideality factor n, and the resistances R_s and R_p can be obtained.

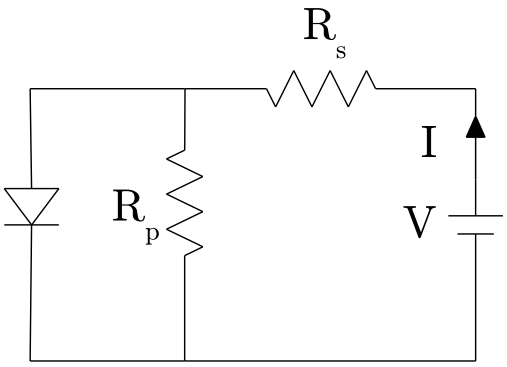

Figure 3.8: Equivalent circuit of the diode measurement.

The height of the energy barrier between the conduction bands of the n-type silicon wafer and the MoO_x layer can be approximated as a Schottky barrier, which is obtained from Eq. (3.2) [23]. Thus, from J_0, the value of the energy barrier can be calculated. This amount quantifies the electron-blocking ability of the layer.

$$J_0 = A^*T^2e^{-\frac{\phi_B}{V_T}} \implies \phi_B = V_T \ln\frac{A^*T^2}{J_0} \quad (3.2)$$

Capacitance-voltage-frequency

The capacitance-bias curve of the diodes can provide information about the built-in voltage of the device by fitting the linear region near 0 V using Eq. (2.17). The defect states of MoO_x induce a capacitance that should be considered when computing the impedance of the device. However, since the response time of these defects is much slower than the one of the p^+n junction, the total impedance can be approximated by the capacitance of the depletion region, C_d, and the dynamic resistance of the diode, $r_d = \left(\frac{dI}{dV}\right)^{-1}$.

3.2.3 Optoelectronic characterization

Quasi-steady state photoconductance

Quasi-steady state photoconductance (QSSPC) is used to measure the effective lifetime of the minority carriers of a semiconductor device. In this technique, a sample is illuminated by a slow varying light pulse (compared to the effective lifetime), and the light-induced excess conductance (photoconductance σ_L) is measured. A coil couples to the conductivity of the wafer, and σ_L is obtained with respect to a reference. From the photoconductance, the average excess minority carrier density can be calculated using the following relation: $\sigma_L = q\Delta n_{\text{av}}(\mu_n + \mu_p)W$, where W is the wafer thickness and the equality $\Delta n = \Delta p$ has been used. Under steady-state illumination, the generation and recombination of electron-hole pairs must be equal, *i.e.* $J_{\text{ph}} = J_{\text{rec}} \implies J_{\text{ph}} = qW\frac{\Delta n_{\text{av}}}{\tau_{\text{eff}}}$. Using the expression for the photoconductance, this can be written as $\tau_{\text{eff}} = \sigma_L \left(J_{\text{ph}}(\mu_n + \mu_p)\right)^{-1}$. Since the mobilities for silicon are known, the generation current is measured by the reference sample, and the photoconductance is measured by the coupled coil, the effective lifetime of the minority carriers as a function of their spatial density can be obtained. More information can be found at [37, 38]

External quantum efficiency

The external quantum efficiency (EQE) is the ratio between the collected charge carriers and the incident photons as a function of the wavelength [2]. The EQE is calculated by illuminating the solar cell with a monochromatic source and measuring the current intensity produced by the solar cell for a range of wavelengths.

As depicted in Fig. 3.9, the EQE is high at wavelengths lower than the gap. However, it is significantly reduced at ultraviolet frequencies because the solar spectra is very low below the UV considering AM1.5. Air mass (AM) 1.5 refers

[2] EQE must not be confused with IQE (internal quantum efficiency), which is the ratio between the collected charge carriers and the absorbed photons.

to the fact that the photons from the Sun go through 1.5 atmospheres in regions such as Europe or USA. The EQE is lower at blue-UV and red-IR wavelengths because the electron-hole pairs generated with photons of these wavelengths are located near the front and rear sides of the Si wafer, which might have a significant surface recombination.

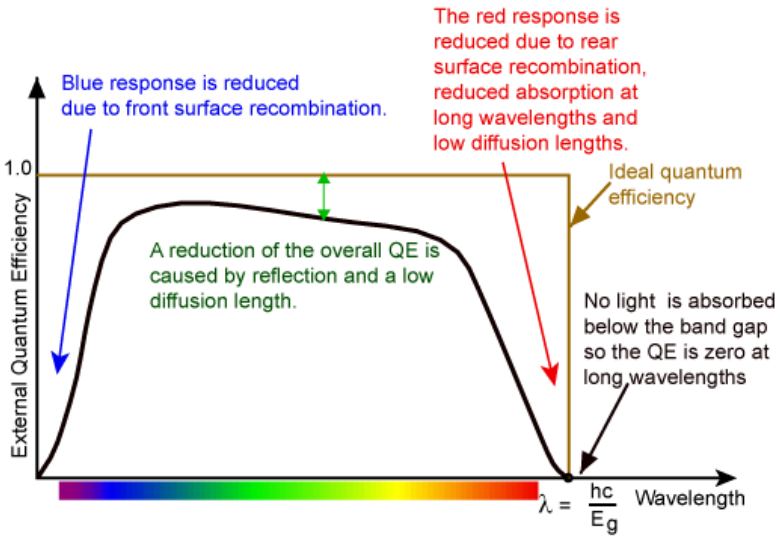

Figure 3.9: External quantum efficiency of a silicon solar cell. Quantum efficiency is usually not measured much below 350 nm as the power from the AM1.5 contained in such low wavelengths is low. Image from [39].

3.2.4 Optical characterization

Ultraviolet-visible spectrophotometry

Ultraviolet-visible (UV-Vis) spectrophotometry measures the transmittance or reflectance of a sample as a function of the wavelength. By using an integrating sphere, both diffuse and specular measurements can be determined.

3.2.5 Structural characterization

X-ray photoelectron spectroscopy

X-ray photoelectron spectroscopy (XPS) is used to determine the atomic composition of a sample's surface. Its operation principle is based on Einstein's photoelectric effect. The sample is irradiated by monoenergetic soft X-rays and the kinetic energy of the emitted electrons is measured. The binding energy E_B of the atomic orbital from which the photoelectron is originated follows that $E_B = h\nu - (K + \phi)$, where $h\nu$ is the photon energy, K is the electron's kinetic energy, and the work

function ϕ represents an adjustable instrumental correction factor that accounts for the energy given up by the electron as it becomes absorbed by the detector. The kinetic energy of electrons is measured by a hemispherical deflection analyzer. By measuring E_B, the specific orbital of the atom from which the electron has been emitted can be known. More information can be found at [40].

Determination of O/Mo ratio. Usually, sample's surface is sputtered with argon so that it is cleaned prior to XPS measurement. However, this technique can also significantly reduce Mo, thus modifying the results of the measurement. A better method involves using fullerene instead of argon, though it is not available at UB installations, which is where XPS measurements were carried out.

As an alternative, in this work surface cleaning has been avoided. Sample's surface XPS spectra was measured, and then the proportion of oxygen bound to Mo was modeled. The oxygen not bound to Mo was approximated to be bound to carbon. Thus, the 1s carbon peak corresponding to the CO bound was analyzed and this contribution was subtracted to oxygen's. Then, the remaining oxygen was considered to be bound to Mo. The position of the peaks can be found in the literature [40].

Chapter 4

Results

4.1 Molybdenum oxide characterization

This work started with the characterization of MoO_x sputter deposition. First, the deposition rate was determined as a function of chamber pressure and RF power. Afterwards, some layers were deposited on c-Si to test their lifetime and how it changed by thermal annealing. Moreover, the optical and electrical characteristics of MoO_x on glass substrates were determined.

4.1.1 Deposition characteristics

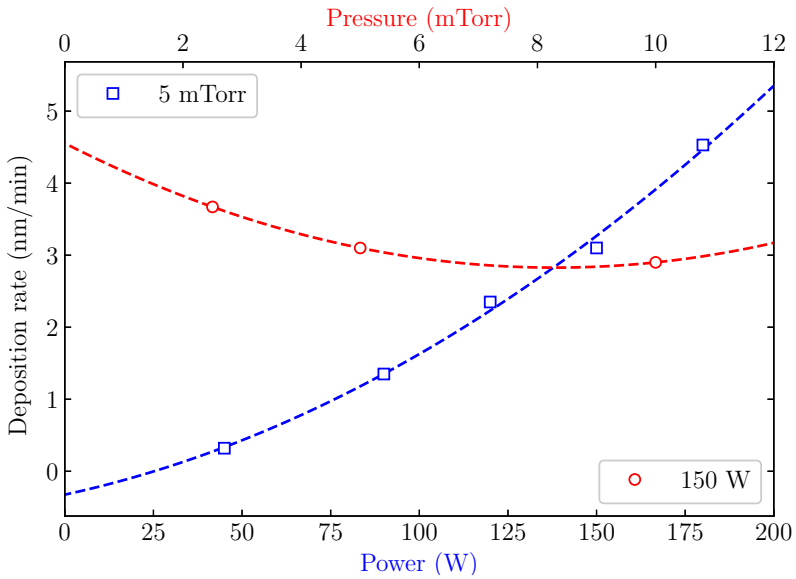

Figure 4.1: Sputter deposition rate of MoO_x vs. pressure and power.

Molybdenum oxide was sputter deposited at an argon flow of 8 sccm (standard cubic centimeters per minute) for different values of chamber pressure and RF source power. The results are shown in Fig. 4.1.

A high deposition rate is desired, and it is achieved by increasing the RF power. However, a large RF power can lead to a high recombinative interface. Thus, a trade-off must exist between the deposition rate and the RF power. In order to combine a high deposition rate with a relatively low RF power, all the MoO_x sputter depositions have been carried out at 150 W and 5.0 mTorr.

4.1.2 Annealing and lifetime improvement

A sample was prepared consisting on a c-Si wafer with a stack of i/n a-Si:H on the rear side and a $\sim$ 50 nm thick MoO_x layer on the front side deposited at room temperature. The effective lifetime of its minority carriers was measured to be 18.9 μs. This sample was annealed at different temperatures with a forming gas (a mixture of hydrogen and nitrogen) flow for 30 minutes. The effective lifetime after each annealing step was measured by the QSSPC method.

As shown in Fig. 4.2, the lifetime initially improves with annealing temperature, until it decays at temperatures higher than 250-300 °C. The improvement can be due to the reduction of MoO_x, which increases its n-type characteristics, and also due to a slight passivation of the MoO_x/c-Si interface. The fact that τ_{eff} starts to decay at annealing temperatures close to 300 °C is most probably due to the degradation of the a-Si stack [41].

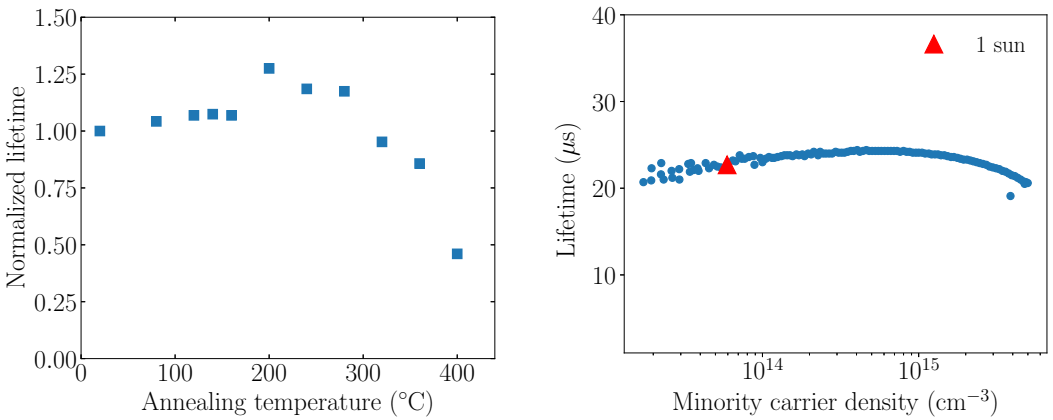

Figure 4.2: Left: Normalized effective lifetime ($\frac{\tau_{\text{eff}}}{\tau_{0,\text{eff}}}$) of a c-Si wafer with a MoO_x layer on one side and an i/n a-Si stack on the other one. The effective lifetime of the device as deposited is $\tau_{0,\text{eff}} = 18.9$ μs. Right: Lifetime vs. minority carrier density of a sample annealed at 200 °C for 30 min. The red triangle refers to 1 sun illumination conditions.

4.1.3 Optical characterization

Transmittance curves were measured for $t \sim 40$nm thick MoO_x layers sputtered on glass for different deposition temperatures ranging from room temperature (RT) up to 400 °C. As shown in Fig. 4.3, the transmittance is lower for films deposited at higher temperatures. Moreover, the measured values are similar for RT/100 °C, and for 200/300 °C, whereas the transmittance for samples deposited at 400 °C is significantly lower. In all cases, bandgap analysis resulted in typical values for glass ($E_g \sim 4$ eV). This could be due to the fact that the MoO_x layers were too thin to detect a significant band-to-band optical absorption.

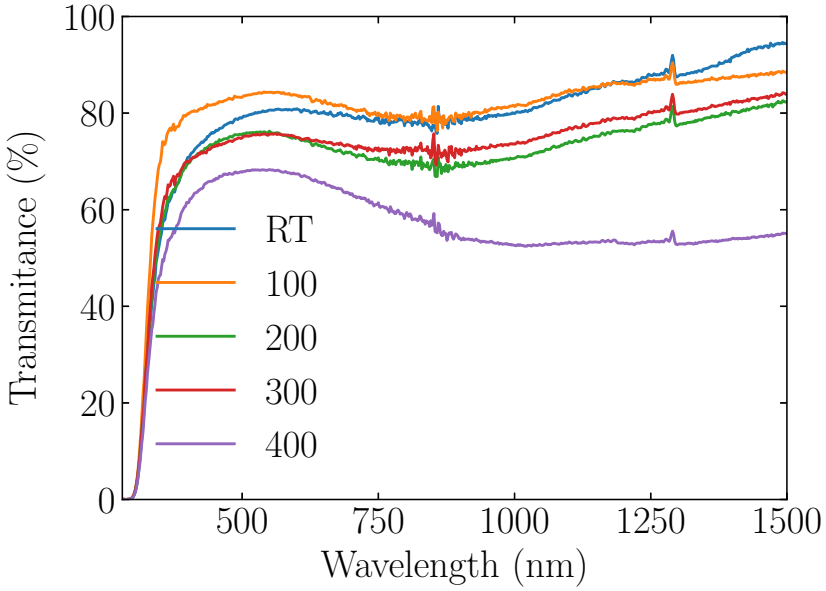

Figure 4.3: Transmittance curves of MoO_x deposited at different temperatures.

4.1.4 Effect of deposition temperature on conductivity

Using TLM technique, sheet resistance of MoO_x layers deposited on glass substrates was calculated. As shown in Table 4.1 and depicted in Fig. 4.4, MoO_x sputter deposited at room temperature (RT) or moderate temperatures such as 100 °C is an insulator –its sheet resistance cannot be even measured. Moreover, although being highly resistive when deposited at 200 and 300 °C, there is a huge improvement of four orders of magnitude down to $R_\square \sim 10$ kΩ/□ for layers deposited at 400 °C.

T_d (°C)	$R_\square$ ($\Omega/\square$)
RT	NM*
100	NM*
200	3.4×10^8
300	1.4×10^7
400	8.1×10^3

Table 4.1: Sheet resistance of MoO_x films deposited at RT, 100, 200, 300 and 400 °C on glass substrate. *NM: not measurable.

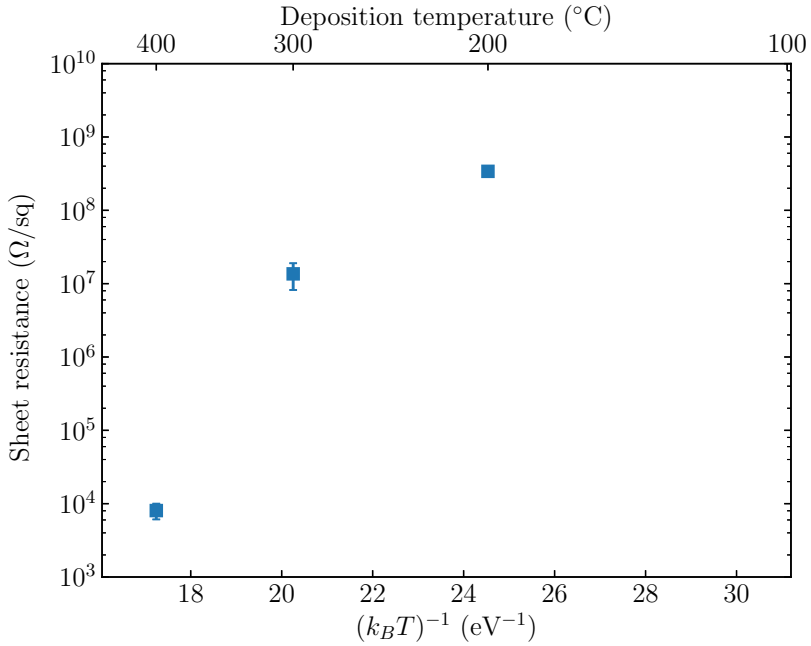

Figure 4.4: Sheet resistance ($R_\square$) of MoO_x deposited on a glass substrate at 200, 300 and 400 °C. $R_\square$ was not measurable for 100 °C and RT samples.

4.2 Molybdenum oxide/silicon heterojunction characterization

In order to determine the effect of MoO_x on c-Si solar cells, samples with MoO_x layers deposited on n- and p-type c-Si wafers were studied. Electrical (TLM and diode) and compositional (XPS) studies were carried out so as to characterize these structures.

4.2.1 Contact and sheet resistances

Electrical characterization of MoO_x was carried out for layers deposited on n- and p-type c-Si. On n-type c-Si, sheet resistance gives information about the inversion layer and thus about the electron blockage of the heterostructure. The R_c value should be as low as possible in order to ensure a good contact with the inversion layer. On the other side, on p-type c-Si the contact resistance provides information about the ability of MoO_x to form an ohmic contact with p-type Si. The sheet resistance should be similar to that of the silicon wafer, *i.e.* $\sim 100\ \Omega/\square$.

In order to characterize the inversion layer of the MoO_x/n-type c-Si heterojunction, sheet resistances have been calculated. If the calculated sheet resistance is sufficiently lower than the one measured for MoO_x on glass (see Section 4.1.4), it can be considered to be the sheet resistance of the inversion layer. Otherwise, the measured sheet resistance is actually the parallel combination of the inversion and MoO_x layers. This has been considered to calculate the $R_\square$ values shown in Fig. 4.5. There, it can be seen that $R_\square$ decreases one order of magnitude for each 100 °C increase in the deposition temperature up to 300 °C. Then, a huge decrease over two orders of magnitude is observed at the highest T_d = 400 °C. Although at 300 °C depositions $R_{IL,\square} \sim 100\text{k}\Omega/\square$ is still far from the $12\text{k}\Omega/\square$ reported by Bullock *et al.* for evaporated MoO_x [17], layers deposited at 400 °C have $R_{IL,\square}$ values lower than 1 $\text{k}\Omega/\square$ –one order of magnitude less than in [17].

Contact resistance values decrease exponentially for MoO_x/n-type c-Si structures, with the value for 400 °C being almost negligible.

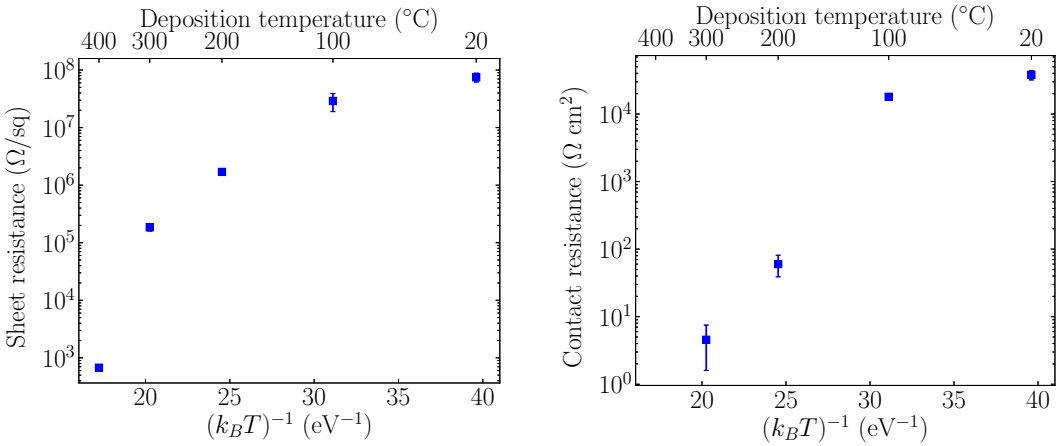

Figure 4.5: Sheet (left) and contact (right) resistance values obtained for MoO_x/n-type c-Si structures at different deposition temperatures.

From $R_{IL,\square}$ values, the inversion layer hole density was computed (shown in Fig. 4.6). Since there is not sufficient inversion with room temperature and 100 °C deposited MoO_x layers, the assumptions used to calculate p are not applicable. Thus, only the values for 200 °C, 300 °C and 400 °C are shown (even the sample at 200 °C seems not to be completely inverted, but it is shown for comparison). The inversion layer hole density value of almost 10^{21} cm^{-3} for 400 °C deposition temperatures is much larger than the one of 8.6×10^{19} cm^{-3} reported for evaporated MoO_x [17]. This result evidences the strong inversion of the Si surface achieved with the MoO_x layers deposited at the highest temperature.

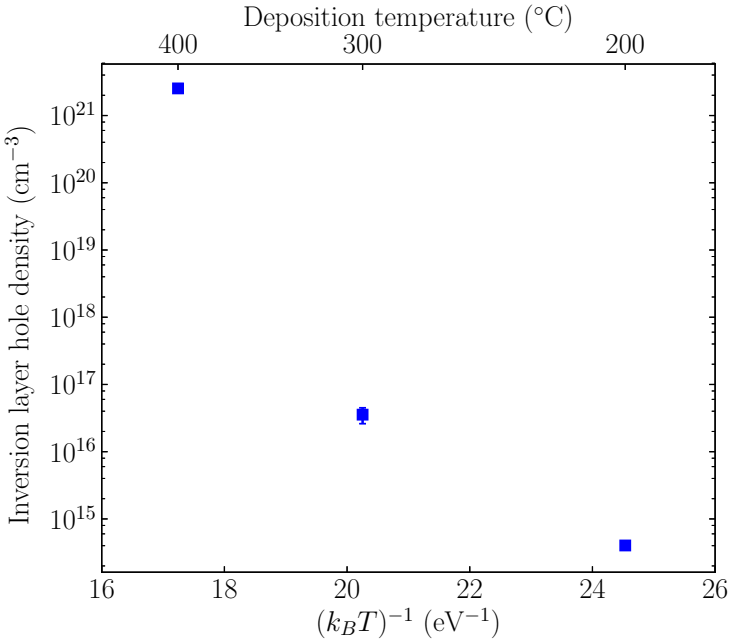

Figure 4.6: Hole density at the inversion layer of n-type c-Si calculated from $R_{IL,\square}$ for different MoO_x deposition temperatures.

As expected, both contact and sheet resistances for MoO_x/p-type c-Si structures are high for room temperature and 100 °C depositions due to the insulator behaviour of MoO_x deposited at these low temperatures. However, contact resistances are less than 0.5 Ωcm^2 for deposition temperatures greater than 200 °C, meaning that a good contact quality to p-type c-Si can be obtained for solar cell fabrication. It is also noticeable that the contact resistance at T_d = 400 °C was again negligible. Besides, the sheet resistance saturates at values near the one of the p-type c-Si wafer.

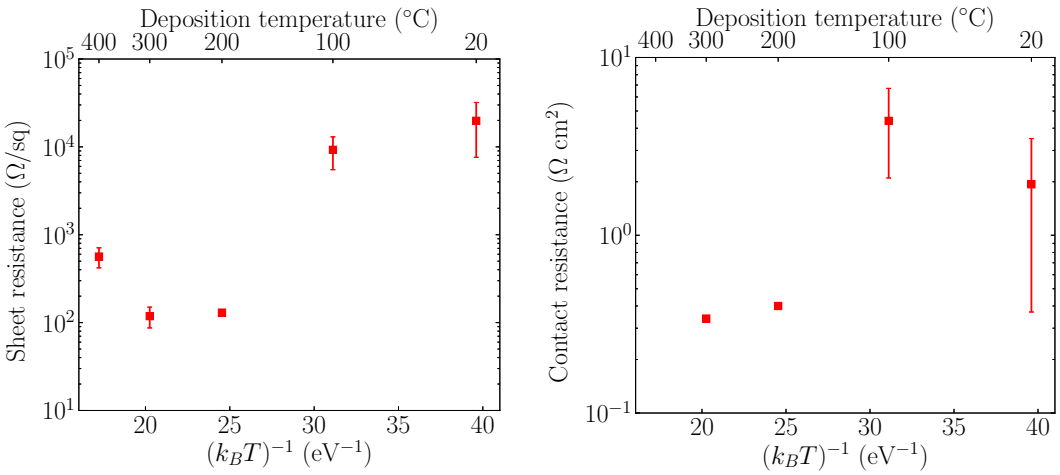

Figure 4.7: Sheet (left) and contact (right) resistance values obtained for MoO_x/p-type c-Si structures at different deposition temperatures.

4.2.2 Diode test devices

Diode test devices were fabricated using Au/MoO_x as front contact and i/n a-Si:H/Al as rear contact as depicted in Fig. 3.7. Current-voltage and capacitance-voltage characteristics were measured in order to further characterize the effect of MoO_x on n-type c-Si wafers.

Current-voltage characteristics

Current-voltage measurements of diodes with MoO_x layers deposited at different temperatures are depicted in Fig. 4.8. From the fitting of these curves, the parameters shown in Table 4.2 are obtained. It is directly seen in the figure that the behaviour for $T_d = \text{RT}, 100$ °C is very similar, with the only noticeable difference being the series resistance, which is obviously greater for $T_d = \text{RT}$ because the MoO_x layer is less conductive at lower deposition temperatures. Analogously, curves for $T_d = 200, 300$ °C are very similar despite R_s being lower for $T_d = 300$ °C. The most noticeable changes are the variations of J_0 with T_d. First, J_0 increases one order of magnitude from $T_d = 100$ to 200 °C. This could indicate an increase in the recombination current. Afterwards, J_0 decreases two orders of magnitude from $T_d = 300$ to 400 °C, probably due to an increase in the barrier height and thus a better electron blockage at the inversion layer.

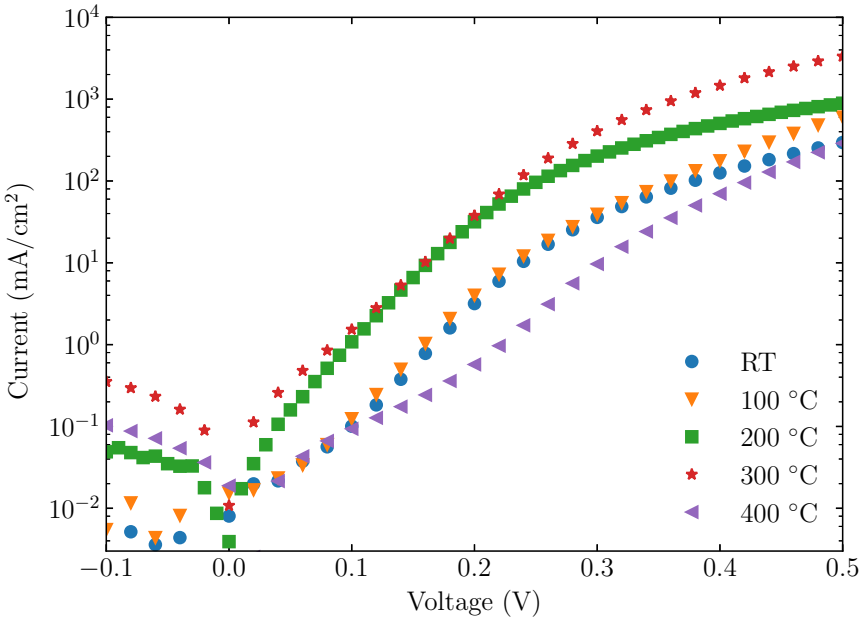

Figure 4.8: Current density-voltage characteristics of fabricated MoO_x/n-type c-Si/i/n a-Si:H diodes for different sputter deposition temperatures.

It should be also noticed that at $T_d = 400$ °C the parallel resistance becomes significant in the diode model. This could be related to the low sheet resistance of the strongly inverted surface in test devices fabricated at the highest T_d.

T_d (°C)	J_0 (mA $\cdot$ cm^{-2})	R_s ($\Omega \cdot$ cm^2)	R_p ($\Omega \cdot cm^2$)	n
RT	2.0×10^{-3}	1.0	∞	1.06
100	2.8×10^{-3}	0.8	∞	1.06
200	2.7×10^{-2}	0.3	∞	1.06
300	3.2×10^{-2}	0.1	∞	1.11
400	5.0×10^{-4}	0.5	1.5×10^3	1.15

Table 4.2: Diode parameters obtained from the fitting of J-V curves for different MoO_x deposition temperatures.

Considering that, when there is inversion, J_0 is mostly due to the performance of the electron-blocking barrier induced by the MoO_x/n-type c-Si heterojunction, the height ϕ_B of this barrier can be approximated as a Schottky barrier. The values of ϕ_B for different deposition temperatures are shown in Fig. 4.9, where it is seen that at $T_d = 400$ °C the barrier height increases to ~ 0.48 V. If recombination currents are of the order of the current due to the Schottky barrier, this approximation is not valid.

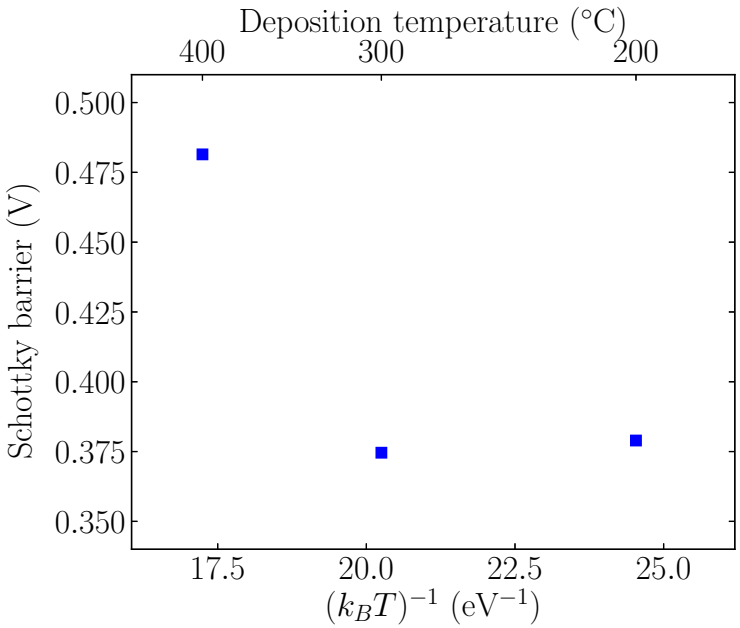

Figure 4.9: Barrier height of the MoO_x/n-type c-Si interface conduction band calculated from J_0 values using the equation for the Schottky barrier.

Capacitance characteristics

Capacitance of the diodes measured at sufficiently high frequencies can be modelled as the capacitance of the depletion region of a p^+n junction. However, this only makes sense when there is an inversion layer –and thus a p^+n junction. It is for this reason that the linear behaviour has not been found for devices with deposition temperatures lower than 300 °C. Fig. 4.10 shows the measured data of a sample with $T_d = 300$ °C alongside the fitting of the linear region. According to the fitting, this sample has a very low built-in voltage (~ 0.2 V).

The equation that relates the built-in potential and the Schottky barrier is $q\phi_B = qV_{\text{bi}} + (E_C - E_F)$ [23]. Using the measured values of $\phi_B \sim 0.4$ eV and $V_{\text{bi}} \sim 0.2$ V, the position of the Fermi level at the n-type c-Si wafer is obtained: $E_C - E_F \sim 0.2$ eV, which is in agreement with the characteristics of the wafer.

The calculated V_{bi} indicates that the open-circuit voltage of solar cells fabricated with MoO_x layers deposited at 300 °C on n-type c-Si will be possibly smaller than the values of 0.7 V obtained with evaporated MoO_x [15]. Unfortunately, capacitance-voltage characteristics for $T_d = 400$ °C could not be measured due to technical problems in the laboratory.

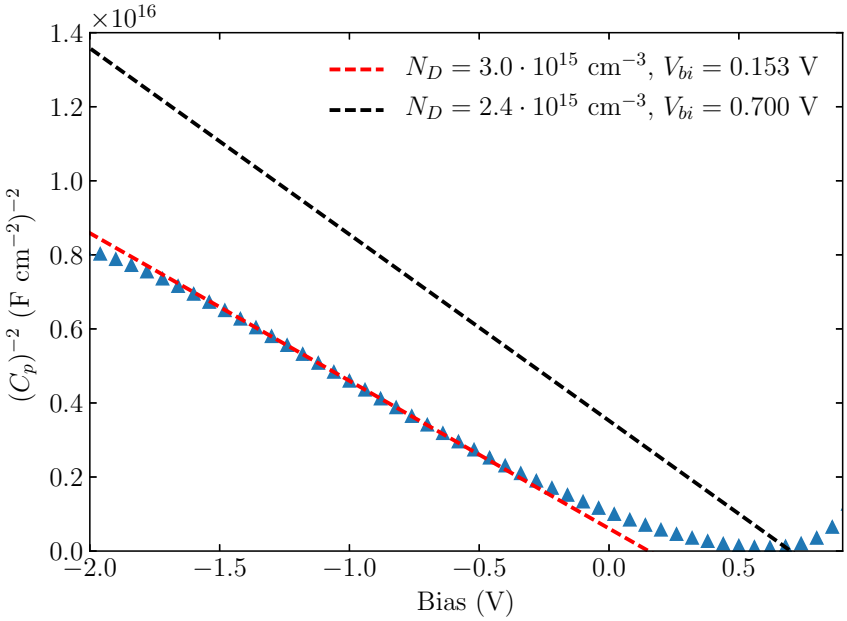

Figure 4.10: Squared inverse capacitance-voltage characteristics of fabricated MoO_x/n-type c-Si/i/n a-Si:H diodes for T_d = 300 °C. The linear region is fitted using the expression for the p^+n junction capacitance. A straight line representing a p^+n junction with $N_D = 2.4 \times 10^{15}$ cm^{-3} (the wafer's dopant) and $V_{bi} = 0.7$ V is shown as reference.

4.2.3 XPS measurements

XPS measurements were carried out in order to investigate the compositional evolution of the MoO_x layers for changing deposition temperatures. In Fig. 4.11, the binding energy region of MoO_3 peaks is shown for layers deposited at different temperatures. In layers deposited at temperatures up to 300 °C, the spectra look the same. Two peaks of the Mo^{6+} oxidized state appear: Mo^{6+} $3d_{3/2}$ at $\sim$ 232.5 eV and Mo^{6+} $3d_{5/2}$ at $\sim$ 236.0 eV. However, at T_d = 400 °C, a peak abruptly appears at $E_B \sim 229.3$ eV, coinciding with the Mo^{4+} $3d_{5/2}$ peak. The Mo^{4+} $3d_{3/2}$ peak, located close to 232.5 eV, broadens the Mo^{6+} $3d_{5/2}$ peak. The position of all the peaks is in agreement with the values reported in the literature [40].

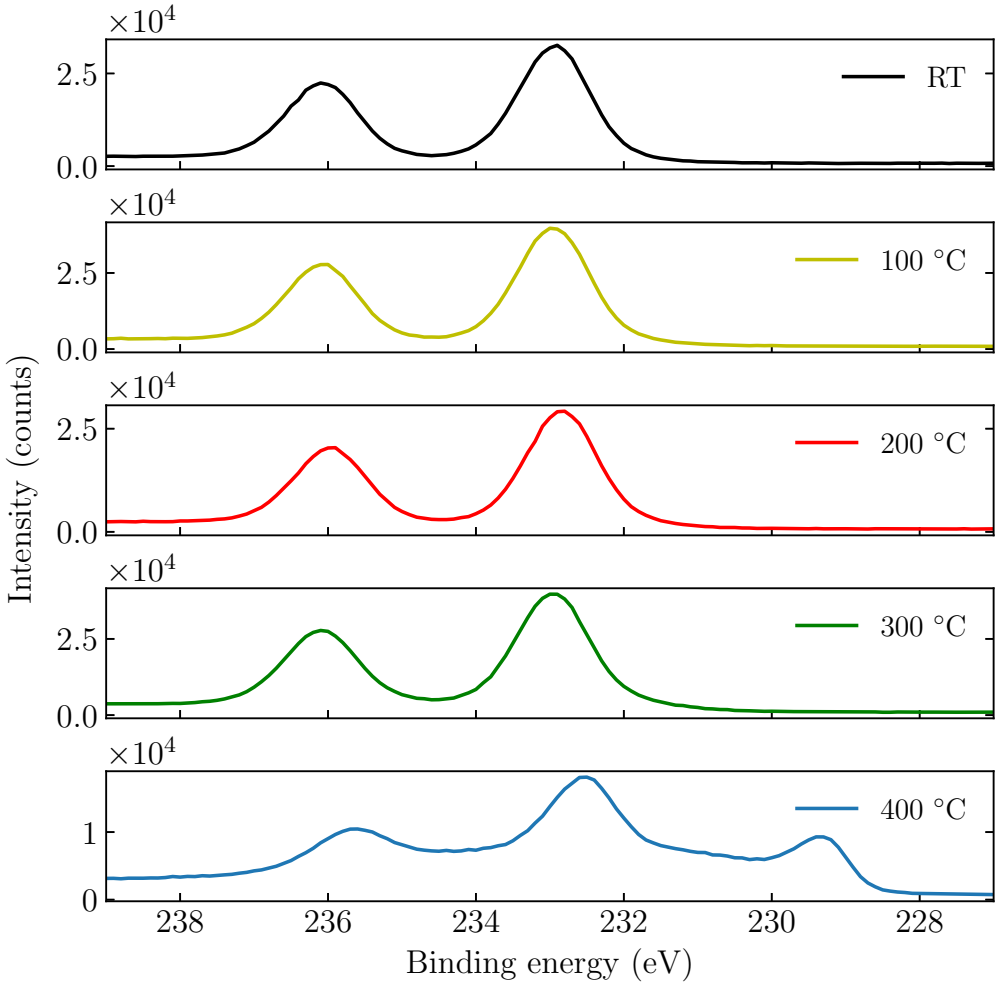

Figure 4.11: XPS spectra of MoO_x deposited at different temperatures. The region shown corresponds to Mo 3d peaks.

From the convolution of both oxygen and molybdenum peaks, the proportion of oxygen atoms bound to molybdenum can be calculated, thus obtaining the x parameter of MoO_x. The results are shown in Fig. 4.12. Although the decrease in the O/Mo ratio is very slight until $T_d = 300$ °C, at $T_d = 400$ °C it significantly decreases, coinciding with the appearance of the Mo^{4+} oxidized state and indicating a transition from MoO_3 to MoO_2.

Notice that suboxidized MoO_x layers ($x < 3$) with semiconducting character are desired for device fabrication. This can be achieved by increasing the deposition temperature.

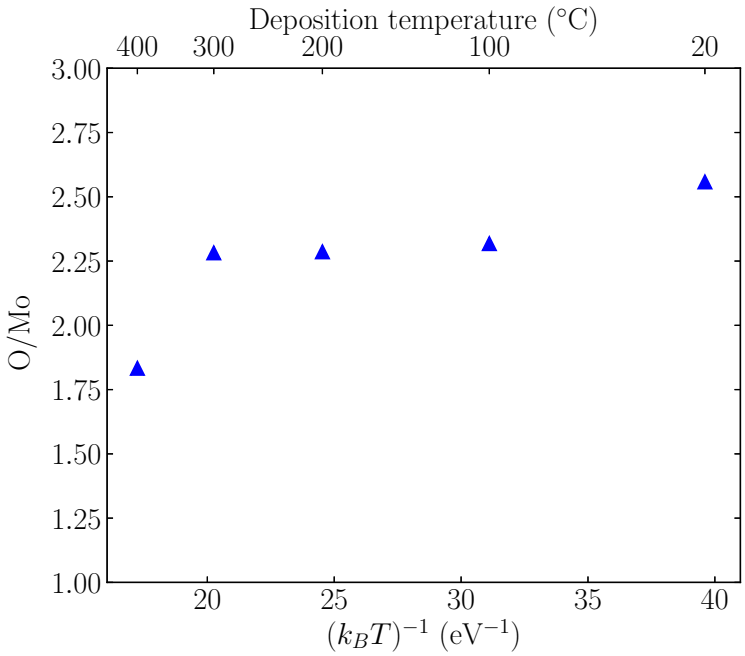

Figure 4.12: Oxygen/molybdenum ratio for different deposition temperatures.

4.3 Solar cell test devices

The behaviour of sputter deposited MoO_x layers on c-Si acting as hole-selective contacts was further studied by fabricating preliminary solar cells using both n- and p-type c-Si wafers. As the electron contact, i/n a-Si:H stacks were used.

4.3.1 Illuminated and dark current-voltage characteristics

At a first stage, solar cells with MoO_x layers deposited at low temperatures (≤ 200 °C) and with different thicknesses were fabricated. The current-voltage characteristics under AM1.5 illumination conditions of solar cells with 10, 25 and 30 nm MoO_x layers are shown in Fig. 4.13. It is noticed that, for thin layers, the photocurrent varies with the bias and, hence, an "S" shape is obtained. However, the "S" shape seems to be corrected when the thickness of the MoO_x layer is increased. This can indicate that a minimum MoO_x layer thickness is required to accumulate enough oxygen vacancies for an efficient hole extraction. Another thing to be noticed is that the open-circuit voltage is very low (~ 0.3 V). This can be due to a combination of two factors: (1) an insufficient –or non-existent– barrier to block electrons, and (2) a highly recombinative MoO_x/n-type c-Si interface.

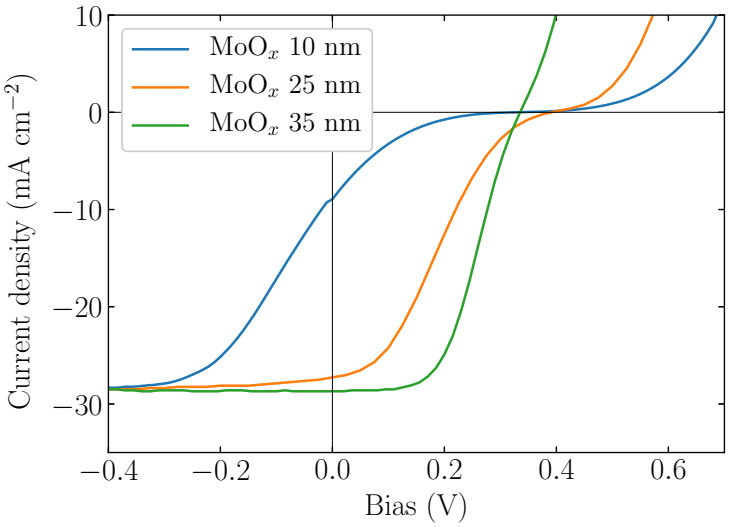

Figure 4.13: Evolution of current-voltage characteristics under illumination for solar cells with MoO_x layers of different thicknesses.

In view of the results obtained from MoO_x characterization, the application of MoO_x to n- and p-type Si-based solar cells was tested by fabricating two solar cell test devices: a T_d = 400 °C sputtered (sp)MoO_x/n c-Si, and a T_d = 300 °C p c-Si/(sp)MoO_x structures with an i/n a-Si:H stack as the electron contact (see Fig. 4.14).

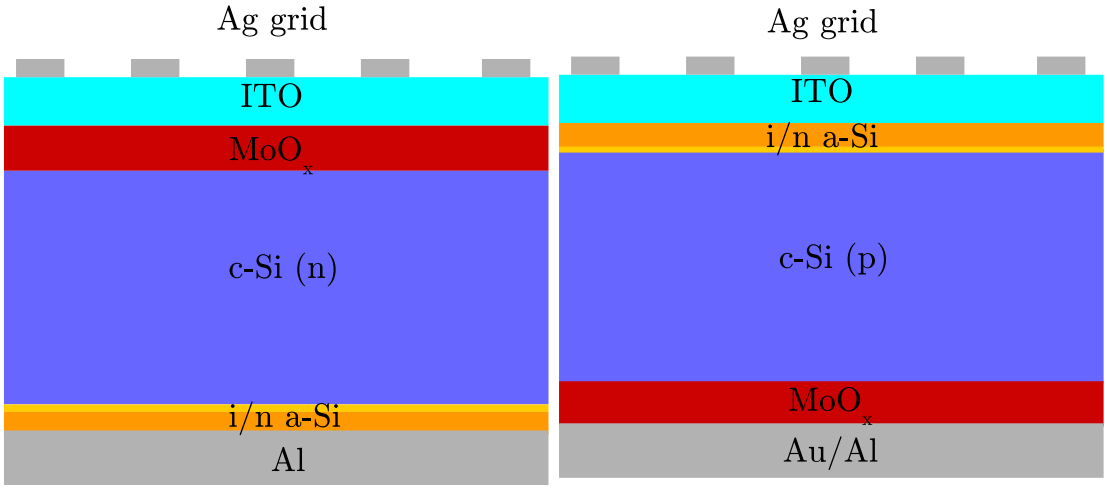

Figure 4.14: Structures of fabricated solar cells on p- (left) and n-type c-Si (right).

Structure	V_{oc} (mV)	J_{ph} (mA $\cdot$ cm^{-2})	FF (%)	η (%)
(sp)MoO_x/n c-Si	340	29.1	52.3	5.2
p c-Si/(sp)MoO_x	480	29.1	55.5	7.8
(ev)MoO_x/n c-Si	610	33.7	73.2	15.0

Table 4.3: Solar cell parameters for the fabricated devices.

The current-voltage characteristics under AM1.5 illumination of these devices is depicted in Fig. 4.15 alongside the curve for a reference evaporated (ev) MoO_x/n c-Si structure. In addition, the parameters extracted from these curves are shown in Table 4.3. Whereas the photocurrent of the fabricated devices is close to the value for devices with evaporated MoO_x, the open-circuit voltage is much lower. In the (sp)MoO_x/n c-Si structure, this can be a combination of two factors: (1) that the rear a-Si:H stack is degraded due to the high temperature of MoO_x deposition [41], and (2) that the high power and temperature of MoO_x deposition contribute to create a very recombinative MoO_x/c-Si interface. In the p-type c-Si/MoO_x structure, V_{oc} is higher because its value is dominated by the front contact (i/n a-Si:H). However, it is still far from the usual 600 mV obtained for good working solar cells. This is probably due to the recombination in the MoO_x/c-Si interface. These problems are also reflected in the fill factor (FF), which is pretty bad compared to the value for devices with evaporated MoO_x.

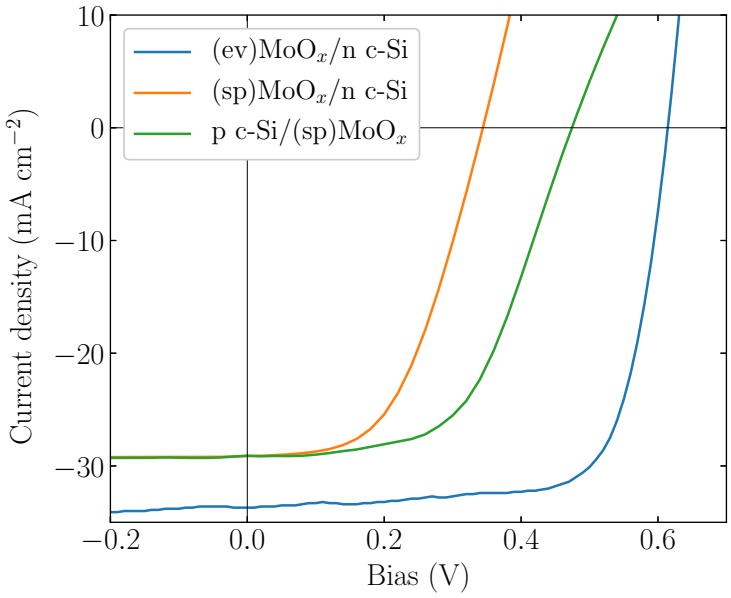

Figure 4.15: Current-voltage characteristics of (sp)MoO_x/n c-Si and p c-Si/(sp)MoO_x alongside data for evaporated (ev)MoO_x/n c-Si solar cells.

Current-voltage characteristics of these devices measured in dark are shown in Fig. 4.16. Some things are extracted from these curves. The J_0 value of (sp)MoO_x/n c-Si solar cell is the largest, indicating a large recombination current. Besides, while (ev)MoO_x-based solar cell curve has the classical two-diode behaviour showing interface recombination dominated ($n \approx 2$ at low injection) and bulk diffusion dominated ($n \approx 1$ at higher voltages) regions, (sp)MoO_x-based solar cells show a more diffuse combination of both, with more presence of the $n \approx 2$ region, indicating that the behaviour of the devices is mostly determined by the recombination at the MoO_x/c-Si interface.

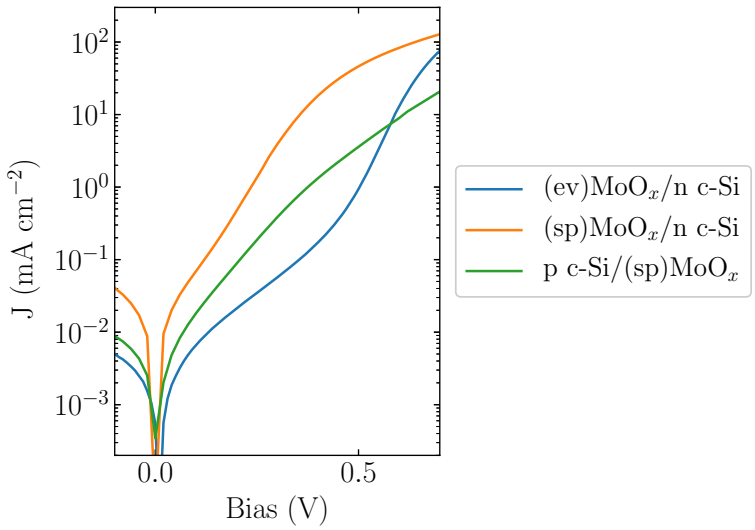

Figure 4.16: Current-voltage characteristics in dark of sputtered (sp) MoO_x/n c-Si and p c-Si/(sp)MoO_x alongside data for evaporated (ev)MoO_x/n c-Si solar cells.

4.3.2 EQE measurements

External quantum efficiency of the fabricated solar cells was measured. The results are shown in Fig. 4.17 alongside the EQE of a reference (ev)MoO_x/n c-Si device. The fact that the area covered for the EQE of (ev)MoO_x/n c-Si is larger is in agreement with a higher photocurrent. Since the rear contact is the same in (sp)MoO_x/n c-Si and (ev)MoO_x/n c-Si, i/n a-Si:H, the infrared response is similar for both devices. However, both (sp)MoO_x/n c-Si and p c-Si/(sp)MoO_x structures provide EQE's at the central region that are lower than the values for (ev)MoO_x/n c-Si. The previous results clearly indicate that this behaviour could be most likely attributed to interface recombination, which is more significant in the (sp)MoO_x/n c-Si structure. Less transparency of MoO_x layers deposited at 400 °C could also cause a decrease in EQE. Additionally, for both (ev) or (sp)MoO_x/n c-Si structures

the response was higher at short wavelengths ($\lambda < 400$ nm). This behaviour is due to the higher transparency of front MoO_x layers compared to a standard a-Si:H heterojunction. The lower EQE of the p c-Si/(sp)MoO_x device at long wavelengths ($\lambda > 1000$ nm) indicates a high interface recombination at the rear surface.

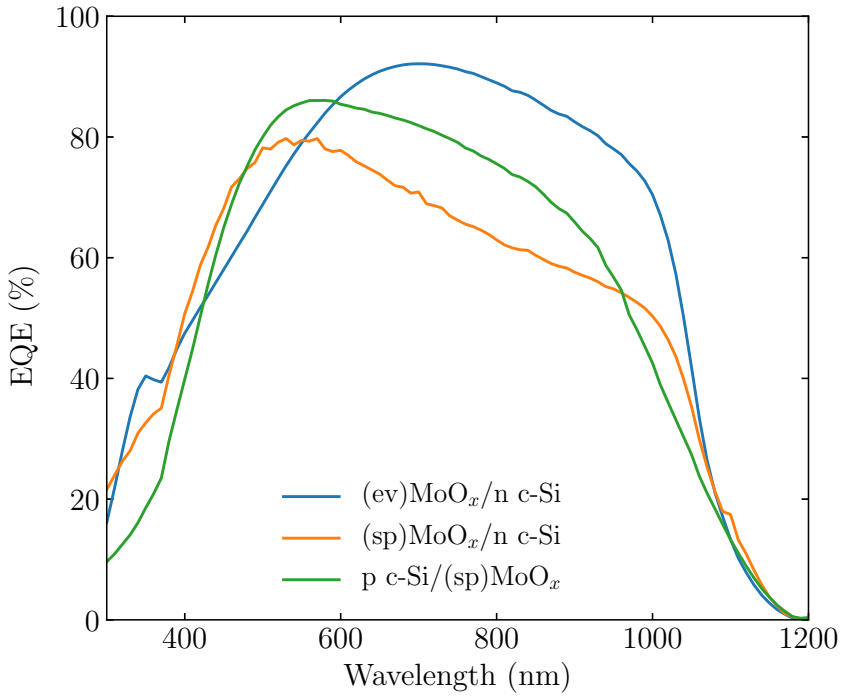

Figure 4.17: External quantum efficiency of (sp)MoO_x/n c-Si and p c-Si/(sp)MoO_x devices alongside data for evaporated (ev)MoO_x/n c-Si solar cells.

Chapter 5

Conclusions

This work has covered a broad range of investigation, starting from the characterization of MoO_x sputter deposition, passing through the characterization of the optical and electronic properties of the material, and ending with the application of the studied technology to fabricate preliminary solar cells.

TLM results have indicated that MoO_x deposited by sputtering using a MoO_3 ceramic target is an insulator at low deposition temperatures. However, its conductivity has been shown to increase progressively with T_d. On n-type c-Si, the inversion layer sheet resistance decreases an order of magnitude each 100 °C step, and a huge drop occurs at $T_d = 400$ °C. The appearance of a MoO_2 peak at the XPS spectra has confirmed that this abrupt increase of the conductivity is related to an increase in the density of MoO_x's oxygen vacancies. Besides, in parallel with the increase of conductivity, the transmittance of MoO_x layers has decreased, probably because of sub-bandgap absorption related to oxygen vacancies. Characterization of fabricated diodes and solar cells has demonstrated that a larger MoO_x conductivity leads to an increase in the MoO_x/c-Si conduction band barrier height and a better hole transport. The idea that a sufficient amount of oxygen vacancies is needed in order to create enough inversion and efficiently extract holes is reinforced by the fact that solar cells with too thin MoO_x layers do not work correctly (Fig. 4.13).

However, several results have shown the limitations of sputtered MoO_x layers. Open-circuit voltage of fabricated solar cells was already predicted to be small by the calculation of the built-in voltage from capacitance-voltage characteristics. Besides, a high J_0 in the diodes' current-voltage characteristics could indicate either a high recombination current or an insufficient electron-blocking barrier height –or a combination of both. While an insufficient barrier height is probable for $T_d < 300$ °C, it achieved a significant value ($\phi_B \sim 0.5$ V) at $T_d = 400$ °C. This confirms that the decrease in J_0 for diodes with $T_d = 400$ °C is due to an improvement of electron-blockage. Nevertheless, J_0 is still too high due to the recombination at

the MoO_x/c-Si interface. That's the reason why V_{oc} of the fabricated solar cells is deteriorated. Besides, EQE characteristics show that, although a better blue response is achieved for MoO_x/n-type c-Si structures due to higher transparency, the overall EQE is reduced because of a higher interface recombination. In regards to p-type c-Si/MoO_x solar cells, the MoO_x layer acts as a rear ohmic hole-contact. The contact resistance has been measured to be very low. The lower EQE values in the infrared ($\lambda > 1000$ nm) are attributable to a highly recombinative interface with the wafer surface.

To sum up, sputtered MoO_x acting as hole-transport layer for c-Si solar cell fabrication works good, but the MoO_x/c-Si interface must be successfully passivated in order to obtain competitive open-circuit voltages. An idea that could explain what is happening is that the combination of high deposition temperature (400 °C) and high RF power (150 W) induces diffusion of molybdenum towards c-Si, creating recombinative centers. A solution to this could be to deposit the MoO_x layers starting with low RF power for the first nanometers and increasing the power to reduce the deposition time without damaging the c-Si surface. However, a better approach would be to use reactive sputtering. Instead of using a ceramic MoO_3 target and parametrizing the deposition temperature to obtain the desired stoichiometry, in reactive sputtering a flow of oxygen would be included in a sputtering chamber in which the target would be metallic Mo. Thus, the parameters to be varied would be oxygen partial pressure and RF power. Certainly, the future of this project is to investigate the application of MoO_x layers deposited by reactive sputtering in c-Si solar cells.

Conference presentations

The work done in this project has given place to poster presentations in conferences, either presenting the results obtained or as collaboration with another project:

- J. Bertomeu, R. Perea, L.G. Gerling, J.M. Asensi, J. Andreu, J. Puigdollers, C. Voz, "Hole-selective contacts by RF magnetron sputtering for heterojunction silicon solar cell structures", 11th Spanish Conference on Electron Devices (CDE), Barcelona, Spain (2017).

- C. Voz, R. Perea, L.G. Gerling, E. Ros, J.M. Asensi, J. Puigdollers, J. Andreu, J. Bertomeu, "Transition-metal-oxide hole-selective contacts by RF magnetron sputtering for heterojunction silicon solar cells", 9th International Conference on Materials for Advanced Technologies (MRS), Singapore (2017).

- J. Puigdollers, L.G. Gerling, G. Masmitja, E. Ros, R. Perea, P. Ortega, C. Voz, R. Alcubilla, "Carrier selective contacts based on V_2O_5-Ag-V_2O_5 structures", European Materials Research Society Spring Meeting (E-MRS), Strasbourg, France (2017).
- J. Puigdollers, L.G. Gerling, G. Masmitja, E. Ros, R. Perea, P. Ortega, C. Voz, R. Alcubilla, "Carrier selective contacts based on dielectric/metal/dielectric structures", 9th International Conference on Materials for Advanced Technologies (MRS), Singapore (2017).

References

[1] S. Shafiee and E. Topal, "When will fossil fuel reserves be diminished?", Energy policy **37**, 181–189 (2009).

[2] C. Rathore and R. Wright, "Monitoring environmental impacts of surface coal mining", International Journal of Remote Sensing **14**, 1021–1042 (1993).

[3] C. L. Carlson and D. C. Adriano, "Environmental impacts of coal combustion residues", Journal of Environmental quality **22**, 227–247 (1993).

[4] D. O'Rourke and S. Connolly, "Just oil? The distribution of environmental and social impacts of oil production and consumption", Annual Review of Environment and Resources **28**, 587–617 (2003).

[5] D. J. Rozell and S. J. Reaven, "Water pollution risk associated with natural gas extraction from the Marcellus Shale", Risk Analysis **32**, 1382–1393 (2012).

[6] R. W. Howarth, R. Santoro, and A. Ingraffea, "Methane and the greenhouse-gas footprint of natural gas from shale formations", Climatic Change **106**, 679 (2011).

[7] A. R. Brandt and A. E. Farrell, "Scraping the bottom of the barrel: greenhouse gas emission consequences of a transition to low-quality and synthetic petroleum resources", Climatic Change **84**, 241–264 (2007).

[8] A. Burnham, J. Han, C. E. Clark, M. Wang, J. B. Dunn, and I. Palou-Rivera, "Life-cycle greenhouse gas emissions of shale gas, natural gas, coal, and petroleum", Environmental science & technology **46**, 619–627 (2011).

[9] D. A. Lashof and D. R. Ahuja, "Relative contributions of greenhouse gas emissions to global warming", Nature **344**, 529–531 (1990).

[10] *Key world energy statistics* (International Energy Agency, 2016), p. 24.

[11] "Photovoltaics Report", Fraunhofer ISE, Freiburg (2016).

[12] K. Masuko, M. Shigematsu, T. Hashiguchi, D. Fujishima, M. Kai, N. Yoshimura, T. Yamaguchi, Y. Ichihashi, T. Mishima, N. Matsubara, et al., "Achievement of more than 25% conversion efficiency with crystalline silicon heterojunction solar cell", IEEE Journal of Photovoltaics **4**, 1433–1435 (2014).

[13]K. Yoshikawa, H. Kawasaki, W. Yoshida, T. Irie, K. Konishi, K. Nakano, T. Uto, D. Adachi, M. Kanematsu, H. Uzu, et al., "Silicon heterojunction solar cell with interdigitated back contacts for a photoconversion efficiency over 26%", Nature Energy **2**, 17032 (2017).

[14]J. Bullock, M. Hettick, J. Geissbühler, A. J. Ong, T. Allen, C. M. Sutter-Fella, T. Chen, H. Ota, E. W. Schaler, S. De Wolf, et al., "Efficient silicon solar cells with dopant-free asymmetric heterocontacts", Nature Energy **1**, 15031 (2016).

[15]C. Battaglia, S. M. De Nicolas, S. De Wolf, X. Yin, M. Zheng, C. Ballif, and A. Javey, "Silicon heterojunction solar cell with passivated hole selective MoO_x contact", Applied Physics Letters **104**, 113902 (2014).

[16]C. Battaglia, X. Yin, M. Zheng, I. D. Sharp, T. Chen, S. McDonnell, A. Azcatl, C. Carraro, B. Ma, R. Maboudian, et al., "Hole selective MoO_x contact for silicon solar cells", Nano letters **14**, 967–971 (2014).

[17]J. Bullock, A. Cuevas, T. Allen, and C. Battaglia, "Molybdenum oxide MoO_x: a versatile hole contact for silicon solar cells", Applied Physics Letters **105**, 232109 (2014).

[18]M. Bivour, J. Temmler, H. Steinkemper, and M. Hermle, "Molybdenum and tungsten oxide: High work function wide band gap contact materials for hole selective contacts of silicon solar cells", Solar Energy Materials and Solar Cells **142**, 34–41 (2015).

[19]L. G. Gerling, S. Mahato, A. Morales-Vilches, G. Masmitja, P. Ortega, C. Voz, R. Alcubilla, and J. Puigdollers, "Transition metal oxides as hole-selective contacts in silicon heterojunctions solar cells", Solar Energy Materials and Solar Cells **145**, 109–115 (2016).

[20]M. T. Greiner, L. Chai, M. G. Helander, W.-M. Tang, and Z.-H. Lu, "Transition metal oxide work functions: the influence of cation oxidation state and oxygen vacancies", Advanced Functional Materials **22**, 4557–4568 (2012).

[21]S. Chuang, C. Battaglia, A. Azcatl, S. McDonnell, J. S. Kang, X. Yin, M. Tosun, R. Kapadia, H. Fang, R. M. Wallace, et al., "MoS_2 p-type transistors and diodes enabled by high work function MoO_x contacts", Nano letters **14**, 1337–1342 (2014).

[22]P. Würfel, *Physics of solar cells: from principles to new concepts* (John Wiley & Sons, 2008).

[23]S. M. Sze, *Semiconductor devices, physics and technology* (Wiley New York, 1985).

[24]U. Würfel, A. Cuevas, and P. Würfel, "Charge carrier separation in solar cells", IEEE Journal of Photovoltaics **5**, 461–469 (2015).

[25]P. A. Cox, *Transition metal oxides: an introduction to their electronic structure and properties*, Vol. 27 (Oxford university press, 2010).

[26]W. Kern, "The evolution of silicon wafer cleaning technology", Journal of the Electrochemical Society **137**, 1887–1892 (1990).

[27]M. Ohring, *Materials science of thin films* (Academic press, 2001).

[28]J. S. Colligon, "Energetic condensation: Processes, properties, and products", Journal of Vacuum Science & Technology A: Vacuum, Surfaces, and Films **13**, 1649–1657 (1995).

[29]D. W. Hess, "Plasma–material interactions", Journal of Vacuum Science & Technology A: Vacuum, Surfaces, and Films **8**, 1677–1684 (1990).

[30]T. F. Consulting, *Fundamentals of sputtering.* `http://www.thfc.de/fundamentals-of-sputtering` (visited on 03/06/2017).

[31]J. S. Chapin, *Sputtering process and apparatus*, US Patent 4,166,018, Aug. 1979.

[32]M. Tanaka, M. Taguchi, T. Matsuyama, T. Sawada, S. Tsuda, S. Nakano, H. Hanafusa, and Y. Kuwano, "Development of new a-Si/c-Si heterojunction solar cells: ACJ-HIT (artificially constructed junction-heterojunction with intrinsic thin-layer)", Japanese Journal of Applied Physics **31**, 3518 (1992).

[33]I. Martın, M. Vetter, A. Orpella, J. Puigdollers, A. Cuevas, and R. Alcubilla, "Surface passivation of p-type crystalline Si by plasma enhanced chemical vapor deposited amorphous SiC_x:H films", Applied Physics Letters **79**, 2199–2201 (2001).

[34]*Dry-etching in photolithography*, (2011) `https://commons.wikimedia.org/wiki/File:Photolithography_etching_process.svg`.

[35]H. Fujiwara, *Spectroscopic ellipsometry: principles and applications* (John Wiley & Sons, 2007).

[36]A. Goetzberger and R. Scarlett, *Research and investigation of inverse epitaxial UHF power transistors*, tech. rep. (DTIC Document, 1964).

[37]D. K. Schroder, *Semiconductor material and device characterization* (John Wiley & Sons, 2006).

[38]R. A. Sinton and A. Cuevas, "Contactless determination of current–voltage characteristics and minority-carrier lifetimes in semiconductors from quasi-steady-state photoconductance data", Applied Physics Letters **69**, 2510–2512 (1996).

[39]*The quantum efficiency of a silicon solar cell.* `http://www.pveducation.org/pvcdrom/quantum-efficiency` (visited on 02/06/2017).

[40]D. Briggs, "Handbook of X-ray Photoelectron Spectroscopy", Surface and Interface Analysis **3** (1981).

[41]S. Dauwe, J. Schmidt, and R. Hezel, "Very low surface recombination velocities on p-and n-type silicon wafers passivated with hydrogenated amorphous silicon films", in Photovoltaic specialists conference, 2002. conference record of the twenty-ninth ieee (IEEE, 2002), pp. 1246–1249.